

Extreme giant molecular clouds in the luminous infrared galaxy NGC 3256

Nathan Brunetti^{*} and Christine D. Wilson

Department of Physics and Astronomy, McMaster University, Hamilton, ON L8S 4M1, Canada

Accepted XXX. Received YYY; in original form ZZZ

ABSTRACT

We present a cloud decomposition of ¹²CO (2–1) observations of the merger and nearest luminous infrared galaxy, NGC 3256. 185 spatially and spectrally resolved clouds are identified across the central $\approx 130 \text{ kpc}^2$ at 90 pc resolution and completeness is estimated. We compare our cloud catalogue from NGC 3256 to ten galaxies observed in the PHANGS-ALMA survey. Distributions in NGC 3256 of cloud velocity dispersions (median 23 km s^{-1}), luminosities ($1.5 \times 10^7 \text{ K km s}^{-1} \text{ pc}^2$), CO-estimated masses ($2.1 \times 10^7 M_{\odot}$), mass surface densities ($470 M_{\odot} \text{ pc}^{-2}$), virial masses ($5.4 \times 10^7 M_{\odot}$), virial parameters (4.3), size-linewidth coefficients ($6.3 \text{ km}^2 \text{ s}^{-2} \text{ pc}^{-1}$), and internal turbulent pressures ($1.0 \times 10^7 \text{ K cm}^{-3} k_{\text{B}}^{-1}$) are significantly higher than in the PHANGS-ALMA galaxies. Cloud radii (median 88 pc) are slightly larger in NGC 3256 and free-fall times (4.1 Myr) are shorter. The distribution of cloud eccentricities in NGC 3256 (median of 0.8) is indistinguishable from many PHANGS-ALMA galaxies, possibly because the dynamical state of clouds in NGC 3256 is similar to that of nearby spiral galaxies. However, the narrower distribution of virial parameters in NGC 3256 may reflect a narrower range of dynamical states than in PHANGS-ALMA galaxies. No clear picture of cloud alignment is detected, despite the large eccentricities. Correlations between cloud properties point to high external pressures in NGC 3256 keeping clouds bound and collapsing given such high velocity dispersions and star-formation rates. A fit to the cloud mass function gives a high-mass power-law slope of $-2.75_{-0.01}^{+0.07}$, near the average from PHANGS-ALMA galaxies. We also compare our results to a pixel-based analysis of these observations and find molecular-gas properties agree qualitatively, though peak brightness temperatures are somewhat higher and virial parameters and free-fall times are somewhat lower in this cloud-based analysis.

Key words: ISM: clouds – ISM: kinematics and dynamics – ISM: structure – galaxies: interactions – galaxies: starburst – galaxies: star formation

1 INTRODUCTION

Understanding the conditions which give rise to varying levels of star formation is an important part of fully describing galaxy evolution over cosmic time. Stellar feedback has dramatic morphological, kinematic, thermodynamic, and chemical impacts on the host galaxy, especially the interstellar medium (ISM). The injection of energy by stars into their surroundings contributes to the turbulent energy that supports the gas disc against gravity, setting the scale height of the atomic and molecular ISM (e.g. McKee & Ostriker 1977; Narayan & Jog 2002; Ostriker & Shetty 2011; Elmegreen 2011; Benincasa et al. 2016; Krumholz et al. 2018). Stellar radiation heats up pockets of the ISM around centres of active star formation through the far-ultraviolet photoelectric effect on polycyclic aromatic hydrocarbons and dust grains (Tielens & Hollenbach 1985; McKee 1989; Hollenbach & Tielens 1999). Mechanically driven shocks from stellar winds and supernovae also contribute to heating the surrounding ISM (McKee & Ostriker 1977; Krumholz et al. 2006; Hopkins et al. 2012). It has been widely shown that the typical rate of star formation within galaxies has dramatically changed over the age of the universe (see e.g. the review by Madau & Dickinson 2014). As the star-formation rate (SFR) in a galaxy changes throughout its life, the

dominance of star formation in driving morphological, kinematic, thermodynamic, and chemical changes will also evolve.

Since the majority of stars form in molecular gas, we focus on exploring the link between the conditions of the molecular gas and the resulting SFR. In particular, we aim to compare the molecular gas properties in nearby spiral galaxies with those within nearby merging galaxies. Mergers cause galaxies to enter a starburst phase (Larson & Tinsley 1978; Ellison et al. 2008, 2013; Hani et al. 2020) in which they exhibit elevated SFRs relative to spiral galaxies as well as relative to their total amount of molecular gas (Daddi et al. 2010; Yamashita et al. 2017; Herrero-Illana et al. 2019; Wilson et al. 2019; Kennicutt & de los Reyes 2021). Therefore, comparing mergers to spiral galaxies in detail will allow us to explore the conditions of the molecular ISM that lead to more vigorous modes of star formation.

Merging systems may also recreate some of the conditions for star formation that existed in high-redshift galaxies. Local merging galaxies have SFRs that are similar to those in high-redshift galaxies (Zaragoza-Cardiel et al. 2018; Larson et al. 2020; Elmegreen et al. 2021, 2009). Additionally, the galaxy merger fraction increases with redshift (e.g. see the compilation and comparison to literature merger fraction estimates spanning $z \lesssim 6$ by Romano et al. 2021). These similarities mean that since we can observe much smaller physical scales in nearby mergers than in high-redshift galaxies, we should be able to link the smaller-scale properties from nearby mergers to

^{*} E-mail: brunettn@mcmaster.ca

the larger scales at high redshift to build a more complete picture of star formation and ISM properties over cosmic time (for a review of the progress made in measuring the properties of the ISM in high-redshift systems see [Tacconi et al. 2020](#)).

At a distance of 44 Mpc (Table 1), NGC 3256 is the nearest luminous infrared galaxy (LIRG), forming stars at a rate of about $50 M_{\odot} \text{ yr}^{-1}$ ([Sakamoto et al. 2014](#)). It is a late-stage merger where the progenitor galaxies' nuclei are still separated but share a common envelope of gas, dust, and stars ([Stierwalt et al. 2013](#)). NGC 3256 also provides, within a single system, a fairly diverse set of environments in which to study molecular gas. The orientation of the northern nucleus appears to be nearly face-on, while the southern nucleus is nearly edge-on (for diagrams see figures 18 and 1 from [Sakamoto et al. 2014](#); [Harada et al. 2018](#), respectively). This edge-on orientation offers a clear view of the spectacular bipolar jet that extends 700 pc north and south of the southern nucleus while only being about 140 pc wide ([Sakamoto et al. 2014](#)). An analysis by [Sakamoto et al. \(2014\)](#) of the energy required to drive the jet indicates it must be at least partially driven by an active galactic nucleus (AGN), consistent with infrared (IR) and X-ray observations ([Ohyama et al. 2015](#)). There is also evidence for a red and blueshifted starburst-powered outflow being launched from the northern nucleus at an angle almost parallel with the line of sight ([Sakamoto et al. 2014](#)).

In this paper we compare clouds identified in carbon monoxide (CO) $J=2-1$ observations of NGC 3256 with clouds found in ten nearby spiral galaxies observed by the Physics at High Angular resolution in Nearby Galaxies with ALMA (PHANGS-ALMA) survey ([Rosolowsky et al. 2021](#)). Details of the observations, imaging, and data preparation are summarized in Section 2. The cloud-finding procedure is described in Section 3, as well as the characterization of cloud-finding completeness. Section 4 covers the main results from comparing our cloud catalogue from NGC 3256 to those from PHANGS-ALMA, and in Section 5 we discuss physical implications of the similarities and differences as well as compare to a pixel-based analysis presented in [Brunetti et al. \(2021\)](#). Finally, we summarize our results and conclusions in Section 6.

2 DATA

2.1 Observations

Observations of the CO (2–1) emission line were carried out towards NGC 3256 with the Atacama Large Millimeter/Submillimeter Array (ALMA) main array, the Atacama Compact Array (ACA), and total power (TP) array. See [Brunetti et al. \(2021\)](#) for a complete description of the observations, calibration, and imaging of the interferometric data. The results were cubes covering the central 6.4 kpc radius of NGC 3256 (or about 130 to 140 kpc^2) from 2004 to 3599 km s^{-1} with 5.131 km s^{-1} wide channels (using the radio convention) with a synthesized beam full width at half maximum (FWHM) of 0.25 arcsec ($\sim 53 \text{ pc}$).

To capture the high velocity outflow and jet present in NGC 3256, the spectral setup of the telescope was arranged such that the edges of two spectral windows (SPWs) covered the CO line to provide a relatively wide bandwidth with high spectral resolution. A fraction of the SPWs overlap in frequency, occurring over the central portion of the spectral line. When reducing the TP observations with the ALMA pipeline, this spectral setup resulted in the two SPWs producing discontinuities in the combined spectra. For this reason the single-dish observations were not combined with the interferometric data in the first paper.

We have since re-attempted reducing the TP observations with the PHANGS-ALMA TP pipeline¹. While this produced a cube of the combined SPWs without obvious discontinuities along the spectra, imaging the two SPWs separately still revealed a maximum difference between beam-averaged intensities of 41 per cent. We estimated the fraction of recovered flux in the original interferometric observations is 90 per cent compared to a cube produced by feathering the interferometric and TP cubes in the Common Astronomy Software Applications (CASA). Given the large difference between the two SPWs that make up the TP cube, and the high recovered-flux fraction in the interferometric cube, we again chose to carry out this analysis on the interferometric-only observations. As a result, the total mass will be underestimated by at most ten per cent, and this bias will be strongest for the spatially-largest clouds.

2.2 Matching resolution and producing uniform-noise cubes

There have been many studies on the biasing effects of differing resolutions and noise levels on cloud decompositions ([Reid et al. 2010](#); [Hughes et al. 2013](#); [Rosolowsky et al. 2021](#)). These studies clearly show that mitigating those differences is essential to making robust comparisons between data sets. Since our primary comparison in this work is to the homogenized cloud catalogue from [Rosolowsky et al. \(2021\)](#) we focus on replicating their procedures as closely as possible. The first step was to correct the cleaned CO cube for the primary beam response. We then convolved this cube to have a synthesized beam FWHM of 90 pc.

To simplify the effects that the noise level in the data has on the recovered mass fraction of each cloud and the cloud-finding completeness, we produced uniform-noise CO cubes following the procedure described by [Rosolowsky et al. \(2021\)](#). Note that we made noise estimates for each pixel in spectral and spatial dimensions following the procedure and parameters used by [Sun et al. \(2018\)](#)² and [Brunetti et al. \(2021\)](#), not the PHANGS-ALMA pipeline used by [Rosolowsky et al. \(2021\)](#).

While our observations of NGC 3256 were roughly the same sensitivity as those of the PHANGS-ALMA sample in Jy beam^{-1} , the greater distance meant we had about ten times higher noise in the Kelvin scale. Since we could not match the noise level of [Rosolowsky et al. \(2021\)](#) (0.075 K across all galaxies after noise homogenization), we tested several noise-level targets and chose to proceed with a value of 0.9 K as it was the lowest noise value that would not exclude clouds due to reducing the usable field of view (FoV). We also note that the observations of NGC 3256 have channels that are about a factor of two wider than the PHANGS-ALMA observations. We will need to be cautious when comparing NGC 3256 and PHANGS-ALMA data sets due to the different noise levels and channel widths.

¹ The scripts can be found at https://github.com/PhangsTeam/TP_ALMA_data_reduction. Accessed 2020 July 14. A modified version made to handle multiple SPWs for a single spectral line will be shared on reasonable request to the corresponding author.

² The PYTHON script for producing noise cubes was obtained from https://github.com/astrojysun/Sun_Astro_Tools/blob/master/sun_astro_tools/spectralcube.py and we used the version at commit f444343.

Table 1. Arguments to *fits2props*.

Argument name	Value
‘distance’	44 Mpc ^a
‘alphaCO’	$1.38 M_{\odot} \text{pc}^{-2} (\text{K km s}^{-1})^{-1}$
‘channelcorr’	0.185
‘minpix’	29
‘sigdiscont’	0
‘compactness’	1000
‘specfriends’	0
‘friends’	0
‘rmstorad’	$\sqrt{2 \ln 2}$
‘bootstrap’	100

^a CMB-corrected redshift retrieved from NED, using *WMAP* five-year cosmology with $H_0 = 70.5 \text{ km s}^{-1} \text{ Mpc}^{-1}$, $\Omega = 1$, and $\Omega_m = 0.27$.

Notes. Used version 1462ff4 of PYCPROPS. Arguments not listed here were left as their default values.

3 ANALYSIS

3.1 Cloud finding

To identify discrete molecular-gas structures in NGC 3256 we used the PYCPROPS³ PYTHON package (Rosolowsky et al. 2021). This package is a translation of the original Interactive Data Language (IDL) CPROPS package (Rosolowsky & Leroy 2006), that takes advantage of the ASTRODENDRO⁴ package for segmenting emission to increase speed as well as other changes to improve robustness for comparative analyses. Rosolowsky et al. (2021) provide a detailed description of the algorithm, so we focus on our parameter choices and how they compare to Rosolowsky et al. (2021).

For the most direct comparison, we use the same criteria for finding maxima as Rosolowsky et al. (2021), which are 1) a minimum contrast between maxima of two times the noise in the cube, 2) a minimum number of pixels that corresponds to one quarter of the beam solid angle, 3) no minimum separation between maxima, and 4) no minimum change in properties from merging maxima. We also set the ‘compactness’ parameter to the same value as Rosolowsky et al. (2021), such that pixels were assigned to produce the most compact structures by the watershed algorithm. Specific arguments to the *fits2props* function are shown in Table 1.

Despite attempting to flatten the noise throughout the CO cube to 0.9 K, as described in Section 2.2, we still calculated a noise cube from the flattened cube to account for any noise variations still present in the data. The median of all pixels in the noise cube was calculated to be 0.897 K and the minimum contrast between maxima was set to the default of two times this median noise. We also chose to use a signal mask when running PYCPROPS to limit the pixels assigned to maxima to only those with likely significant emission. This signal mask was produced from the flattened-noise cube with the same script used to make the noise cubes. We note that the procedure to generate the noise and signal-mask cubes was not identical to the PHANGS-ALMA pipeline, used by Rosolowsky et al. (2021), but they were designed by Sun et al. (2018) to be used for the same purposes (E. Rosolowsky, private communication).

PYCPROPS requires an estimate of the channel-to-channel correla-

tion to remove the finite channel response from the velocity dispersions of the clouds. We estimate this correlation from emission-free channels with the Pearson correlation coefficient calculated from all pixel values between the i and $i + 1$ channels (the ‘channelcorr’ argument). Internally, PYCPROPS estimates major and minor axis lengths for each cloud and combines these into a single radius for each structure, R . This radius is calculated as $R = \eta \sqrt{\sigma_{\text{maj,d}} \sigma_{\text{min,d}}}$ (equation 9 from Rosolowsky et al. 2021) where $\sigma_{\text{maj,d}}$ and $\sigma_{\text{min,d}}$ are the major and minor sizes, assumed to be the spatial standard deviations of Gaussian clouds, and η is a factor that depends on the mass distribution within the cloud. η corresponds to the ‘rmstorad’ argument to *fits2prop* in Table 1 and we have adopted the same value of $\sqrt{2 \ln 2} \approx 1.18$ as used by Rosolowsky et al. (2021), corresponding to a Gaussian density profile and assuming R is the half width at half maximum (HWHM) of the cloud.

Cloud finding was carried out at 90 pc resolution to simplify comparisons to results from Rosolowsky et al. (2021), and this resolution can also be roughly compared to the 80 pc resolution pixel-based analysis from Brunetti et al. (2021). However, instead of using cubes regridded to have pixels that were half the beam FWHM, as done by Brunetti et al. (2021), we kept the original pixel grid from the original cleaned cube. This was because we found an unexpected trend of increasing cloud velocity dispersion distributions with decreasing pixel size. See Appendix A for details of the tests which showed this behaviour.

3.2 Estimating source-finding completeness

Interpretation of the cloud-property distributions measured in NGC 3256 depends on understanding the impact that the noise level, resolution, and choice of cloud-finding algorithm have on the types of clouds we are able to find. To empirically infer the completeness limits on our cloud finding we performed Monte Carlo tests by injecting 1200 synthetic sources with unique properties into our data, one at a time, and attempted to find them with the same steps described in Section 3.1. We recorded if the injected sources were found as well as the cloud properties estimated by PYCPROPS.

We chose to inject sources into a subset of channels at the high-velocity end of the original emission cube that did not contain significant real emission. This process simplified the interpretation of the source-finding results since any clouds found would be attributed to the injection of the synthetic source. However, a limitation is that the effect of source blending is not incorporated in our completeness estimate. Blending of clouds likely plays a non-trivial role as most of the emission in NGC 3256 is interconnected through the cube with few instances of isolated “islands” of emission.

It is worth noting that the procedure for finding synthetic clouds was not exactly identical to cloud finding in the real emission. The difference was that instead of recalculating the noise cube after injecting each source, we used the noise cube from the original source finding, trimmed to the same channels as the emission cube. We found that recalculating the noise cube from just that subset of channels resulted in subtle noise structures across the FoV not appearing in the resulting noise cube. These structures appeared to be originating from channels with significant emission, which explained why they were missing in the recalculated synthetic-source noise cube. We chose to preserve the effects that the real emission was having on the noise cube over any that would be introduced when the synthetic sources were injected.

To choose the synthetic source properties, we followed Rosolowsky et al. (2021) by uniformly sampling (in log-space) cloud masses, surface densities, and virial parameters. The distributions of

³ <https://github.com/PhangsTeam/pycprops>

⁴ <http://www.dendrograms.org/>

these properties were centred on $2 \times 10^7 M_{\odot}$, $600 M_{\odot} \text{pc}^{-2}$, and 7 with widths of 2.75, 2, and 2.25 dex, respectively. The ranges of synthetic properties were chosen such that the upper limit is about two times the largest value from our cloud catalogue and the lower limit is about half the smallest. Masses, surface densities, and virial parameters were used to calculate three-dimensional Gaussian parameters corresponding to the spatial and velocity standard deviations. These Gaussian parameters were then added, in quadrature, to the beam standard deviation or equivalent Gaussian channel width ($\sigma_{v,\text{chan}}$ in equation 6 from Rosolowsky et al. 2021) to replicate the effects of resolution on the synthetic clouds' true properties. Peak brightness temperatures were then calculated from the mass and ‘‘convolved’’ spatial and spectral sizes still following the three-dimensional Gaussian cloud model of Rosolowsky et al. (2021). Position-position-velocity (PPV) Gaussians were calculated from these parameters and were added to the emission cube.

For each of the 1200 choices of properties we also chose to separately inject and search for five identical sources that were centred at different right ascension (R.A.), declination (Dec.), and velocity positions. By injecting identical sources at different locations we reduce the stochastic nature of sources being more easily found (missed) if placed on a noise peak (trough). Five positions were uniformly drawn from ranges of R.A., Dec., and velocity, and each choice of cloud properties was injected at those five locations. The R.A. and Dec. ranges were limited to a region whose centre coincides with the centre of the FoV, with a width of 7.25 kpc in R.A. and height of 4.5 kpc in Dec.. Placing the synthetic sources within this region ensured the centres of the largest synthetic clouds were at least two spatial standard deviations from the mapped edges. Similarly, the number of channels that made up the subset of the cube in which synthetic sources were injected was chosen to cover a velocity range corresponding to $\sim 1\sigma_v$ for the largest synthetic cloud velocity width chosen, and the velocity centres were chosen to be ~ 0.4 velocity standard deviations from the edge channels.

Figures 1 and 2 summarize the results of our completeness estimation. Each point in Figure 1 represents a combination of cloud properties chosen in the mass-surface density-virial parameter space. In Figure 2 the results are shown converted to the observable peak brightness temperature-velocity dispersion-2D radius cloud property space (before applying the effects of resolution). The colours of the points indicate how many of the five unique positions were found by PYCPRIPS such that regions of high and low completeness are the yellow and purple regions, respectively. The coupled nature of the properties shown in Figure 1 is apparent as no single property, or even pair of properties, straightforwardly determines the likelihood a cloud will be found. The observational constraints are clearer in Figure 2, primarily in the peak brightness temperature-radius plane, where the likelihood of a cloud being found depends strongly on the part of parameter space in which it appears. The boundary between detectable and not-detectable clouds is similarly sharp in the mass-surface density-virial parameter space but is not as clear when the results are projected into the panels of Figure 1.

Following Rosolowsky et al. (2021), we perform a binomial logistic regression through maximum likelihood estimation to fit the

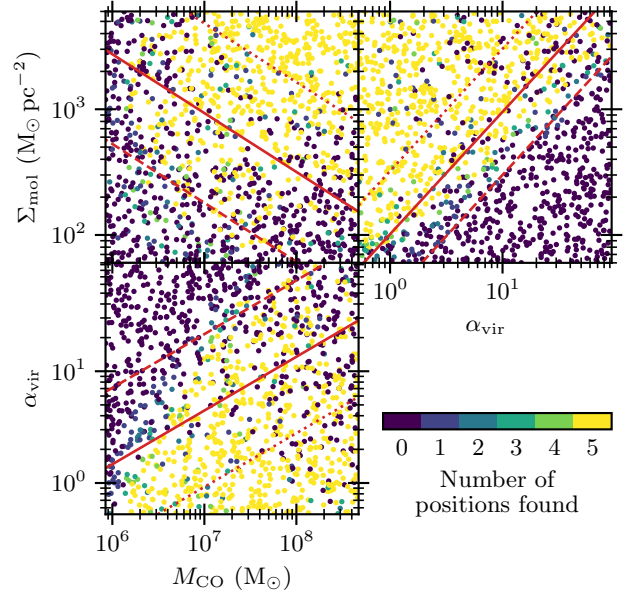


Figure 1. Results of Monte Carlo completeness tests from injecting synthetic sources with 1200 unique cloud properties chosen from log-uniform distributions of mass, surface density, and virial parameter. Each point represents one choice of cloud properties. Each choice of properties was injected five separate times into the cube at different R.A., Dec., velocity positions and PYCPRIPS was run to attempt to find each source. The colours of the points indicate how many of the five different positions had at least one cloud found by PYCPRIPS. Red lines indicate the predicted 80 (dotted), 50 (solid), and 20 (dashed) per cent completeness contours after averaging the three-dimensional fit along the axis not shown in each of the panels.

completeness results with the function

$$P(M, \Sigma, \alpha_{\text{vir}}) = \left\{ \begin{aligned} & 1 + \exp \left[\begin{aligned} & -c_0 \\ & -c_1 \log_{10} \left(\frac{M}{10^6 M_{\odot}} \right) \\ & -c_2 \log_{10} \left(\frac{\Sigma}{150 M_{\odot} \text{pc}^{-2}} \right) \\ & -c_3 \log_{10} \left(\frac{\alpha_{\text{vir}}}{2} \right) \end{aligned} \right] \end{aligned} \right\}^{-1} \quad (1)$$

with the best-fitting parameters and 95 per cent confidence intervals (CIs) summarized in Table 2. To be clear, the fit is not done to the fraction of positions detected for each choice of cloud properties. Instead, for each combination of mass, surface density, and virial parameter (the independent variables) the dependent variable is either zero to mark no clouds found or one to mark at least one cloud found. With a functional form for the completeness we calculated a grid of completeness predictions over our range of synthetic source properties and plot the 80, 50, and 20 per cent completeness contours in Figures 1 and 2, averaged along the third axis not shown in each panel.

The velocity dispersion vs. radius panel in Figure 2 appears to

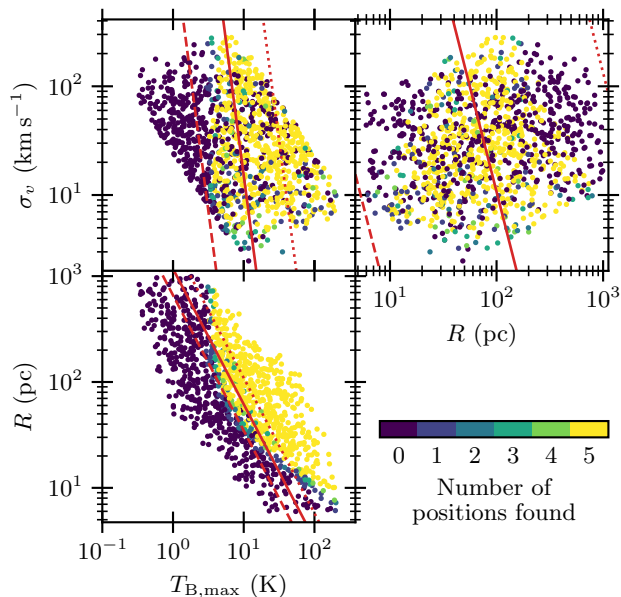


Figure 2. Same as Figure 1 but with the cloud properties converted to the observable properties of peak brightness temperature, velocity dispersion, and radius. To calculate the Gaussian PPV synthetic sources injected for the completeness tests, these values of R and σ_v are first combined with the beam and channel width, respectively, to emulate observational effects. Then the $T_{B,\max}$ values are recalculated from these “observed” R and σ_v values, and finally the Gaussian source is calculated from these properties. The velocity dispersion vs. radius panel appears to have its fitted completeness trend rising in the opposite direction to the scatter-point colours; see discussion in Section 3.2.

Table 2. Results of logistic regression fit to completeness results. Estimated parameters correspond to those in Equation 1.

Parameter	Best-fitting value	Lower 95% CI	Upper 95% CI
c_0	-2.8	-3.1	-2.6
c_1	1.8	1.7	2.0
c_2	3.9	3.7	4.1
c_3	-3.8	-4.0	-3.6

have its fitted completeness trend rising in the opposite direction to the scatter-point colours. However, this is due to different ranges of velocity dispersion and radius being probed by our completeness tests at different values of peak brightness temperature. If the scatter points are limited to a narrow range of temperatures then both the points and the fit trend show generally lower completeness for combined small radii and velocity dispersions and high completeness for large radii with high velocity dispersions. Ultimately, the combination of velocity dispersion and radius alone is not a strong predictor of completeness.

Properties estimated by PYCPRPS for the synthetic sources were compared to the known values used to inject the sources, over ranges similar to the range of properties estimated for clouds found in the original CO cube. The values from PYCPRPS are those for which an attempt to remove the effects of finite sensitivity and resolution have been applied (see section 3.4.2 of Rosolowsky et al. 2021 for details of how these corrections are done), and we compare with the input synthetic cloud properties before they are adjusted for the

effects of resolution. The ratio of total recovered luminosity to the input luminosity is about 0.7, on average, with a standard deviation near 0.2. When considering found clouds with the largest fraction of the luminosity, the ratio of estimated radii relative to input radii also averages around 0.7 with a standard deviation of about 0.2. The same comparison for velocity dispersions shows a ratio of about 0.8, on average, with a standard deviation around 0.3. These biases and spreads are consistent with those reported by Rosolowsky et al. (2021) for the PHANGS-ALMA data.

4 RESULTS

In this section we summarize the cloud properties measured in NGC 3256 and compare to the cloud properties in PHANGS-ALMA galaxies. Samples only include clouds that could be both spatially and spectrally deconvolved from the resolution of the observations (performed internally by PYCPRPS).

4.1 Two-dimensional model of clouds

Figure 3 compares the distributions of cloud properties between NGC 3256 and each PHANGS-ALMA galaxy, estimated directly from the PYCPRPS measurements⁵. Note that all Gaussian kernel density estimator (KDE) bandwidths presented here were automatically calculated using the SCIPP implementation of Scott’s Rule (Scott 1992), and that uniform weights were used for all clouds. Most properties are significantly larger in NGC 3256 than most or all of the clouds identified by Rosolowsky et al. (2021) (velocity dispersion, luminosity, CO-estimated mass, and mass surface density). Smaller differences are present for the distributions of on-sky radii, and no significant differences appear in the distributions of estimated cloud eccentricities. Medians and inner 68th percentiles are shown as circles and errorbars, respectively, but the means are very similar to the medians for all galaxies and properties. It is worth noting that the uncertainties on the means would appear smaller than the circles such that the mean for nearly every galaxy is significantly different from every other galaxy.

We used a single U/LIRG type conversion factor $\alpha_{\text{CO}(2-1)} = 1.38 M_{\odot} \text{pc}^{-2} (\text{K km s}^{-1})^{-1}$ for NGC 3256 (see Brunetti et al. 2021, for a description of how we decided this was appropriate). For PHANGS-ALMA, a metallicity-dependent conversion factor was used based on radial metallicity gradients from Sánchez et al. (2014, 2019) and described in detail by Sun et al. (2020a). All conversion factors for the PHANGS-ALMA clouds were larger than the value we used for NGC 3256, with a median of $\approx 6.75 M_{\odot} \text{pc}^{-2} (\text{K km s}^{-1})^{-1}$, such that all PHANGS-ALMA luminosities were scaled up by a larger factor to convert to masses than NGC 3256. Switching our choice of conversion factor for NGC 3256 to that of the Milky Way would result in the masses increasing by a factor of ~ 4.5 , with the horizontal arrow in Figure 3 showing this change.

The most important comparisons are between the directly-observable properties (cloud size, velocity dispersion, peak brightness temperature, and luminosity), since the other properties are each derived from the former. However, given the galaxy-specific scatter in the relations between these cloud properties (some of which are presented in Figures 9 through 12) we also show properties like mass

⁵ The electronic table of clouds found by Rosolowsky et al. (2021) was retrieved from the journal website on 2021 July 31.

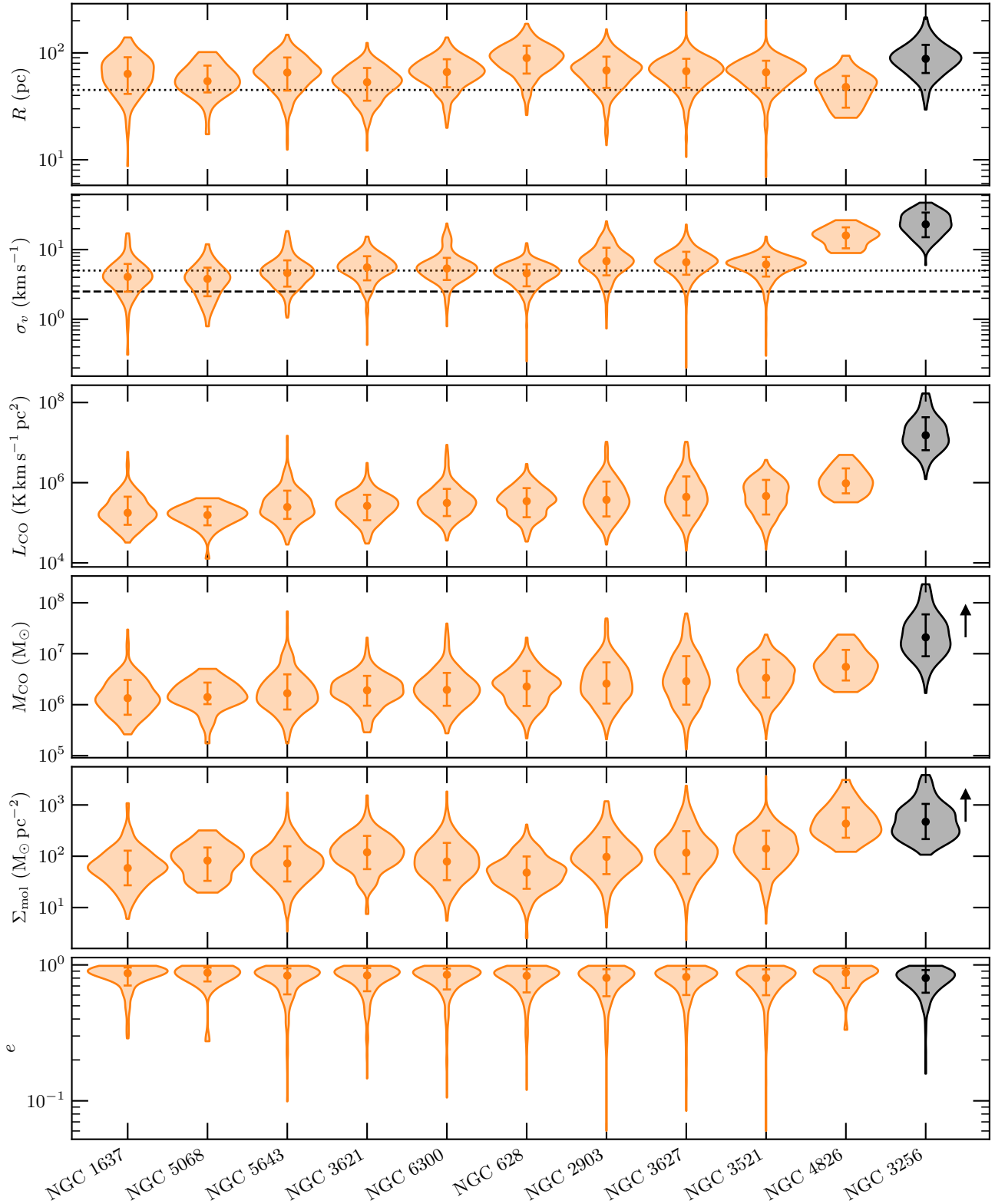


Figure 3. Resolved cloud-property distributions for NGC 3256 and the PHANGS-ALMA sample. Circles show medians and errorbars show 16th to 84th percentile ranges. Curves and shaded regions show Gaussian KDEs, with uniform weights for all clouds. The widths are normalized for each parameter to show relative cloud fractions per dex between galaxies (i.e. the area of the shaded regions is the same for each galaxy). Galaxies are sorted from low (left) to high (right) median cloud mass. The beam HWHM of 45 pc is shown with the dotted line in the R panel. Dotted and dashed lines in the σ_v panel show channel widths of 5 km s⁻¹ for NGC 3256 and 2.5 km s⁻¹ for PHANGS-ALMA, respectively. Masses and mass surface densities in NGC 3256 are estimated with a U/LIRG α_{CO} of 1.38 M_⊙ pc⁻²(K km s⁻¹)⁻¹ (others with the Milky-Way value). Multiplying the masses and mass surface densities in NGC 3256 by ~ 4.5 would switch those values to using the Milky Way conversion factor, with these shifts shown by the arrows.

surface density and eccentricity that are derived through combinations of the observables. Finally, due to the lack of published peak brightness temperatures for the PHANGS-ALMA clouds, we cannot present a comparison of this property (though we do include it for NGC 3256 in Table 4 and Figure 13).

There is substantial overlap between the two-dimensional radii estimated for clouds in NGC 3256 and the PHANGS-ALMA galaxies, but the distribution for NGC 3256 extends to larger radii than most PHANGS-ALMA galaxies. The cloud-radius distribution in NGC 3256 is very similar to that in NGC 628, both of which exhibit the largest clouds shown here. The sizes of clouds in NGC 3256 are also noteworthy because nearly all radii are significantly larger than the beam HWHM, shown as the dotted line in Figure 3. Source-finding algorithms built on emission segmentation, such as PYCPROPS, typically identify peaks of emission near the size of the beam (Pineda et al. 2009; Hughes et al. 2013; Leroy et al. 2016; Reid et al. 2010; Rosolowsky et al. 2021), which is clearly apparent for many of the clouds in the PHANGS-ALMA galaxies.

Given the matched resolution to the PHANGS-ALMA cloud-finding analysis, identical source-finding algorithm, and similar treatment of signal and noise portions of our cube it appears the difference in the sizes of molecular gas structures between NGC 3256 and most PHANGS-ALMA galaxies is real. The difference in noise between our observations of NGC 3256 and those from PHANGS-ALMA could result in differences in the measured cloud sizes. However, noise levels have been shown to be anti-correlated with measured cloud size for clouds estimated to be the size of the beam or larger (Rosolowsky & Leroy 2006), which 96 per cent of our resolved clouds from NGC 3256 are. Bias related to higher noise would be making the clouds from NGC 3256 appear smaller than they actually are so that the difference from the PHANGS-ALMA galaxies is more likely to be larger than estimated here rather than smaller.

Nearly all clouds in NGC 3256 have velocity dispersions well above our spectral resolution of $\approx 5 \text{ km s}^{-1}$ (no clouds have velocity dispersions less than the channel width). The same is true for most galaxies from PHANGS-ALMA, except for NGC 5068 where ≈ 27 per cent of resolved clouds are estimated to have dispersions below their spectral resolution of 2.5 km s^{-1} . The majority of clouds from NGC 3256 have velocity dispersions significantly larger than clouds from PHANGS-ALMA. However, the upper half of the distribution from NGC 4826 overlaps with the lower half of the distribution from NGC 3256.

Both the noise level and channel width are complicating differences between the velocity-dispersion measurements of NGC 3256 and PHANGS-ALMA. Rosolowsky & Leroy (2006) showed that velocity dispersions are overestimated in the presence of finite-width channelisation, by about 15 per cent for high-signal-to-noise (S/N) clouds when the true velocity dispersions are equal to the channel width. This bias rapidly increases for dispersions smaller than the channel width (see their figure 1). They also explored varying the noise level relative to the cloud peak intensity, showing that overestimating the velocity dispersion was worse at lower S/N. For example, the same 15 per cent bias occurred for clouds with true dispersions about twice the channel width at a S/N of about 5.

If we assume the measured velocity dispersions from the PHANGS-ALMA galaxies are their true dispersions and use the estimates of velocity-dispersion bias from Rosolowsky & Leroy (2006) for clouds with S/N of only 5, then we estimate the channels would have to be about 15 km s^{-1} wide to shift the median dispersions to be roughly the same as measured in NGC 3256. Including clouds with a range of S/N values above five would require even wider channels (the PHANGS-ALMA S/N values were not published but we have

included them for NGC 3256 in Tables 4). Also, the distributions are extremely narrow, making the PHANGS-ALMA distributions look nothing like the wide distribution measured in NGC 3256. While the differences between noise and channel width do not appear to be the obvious direct drivers of the differences in cloud size and velocity dispersion, these comparisons would be best explored by altering the PHANGS-ALMA cubes to have the same noise and channel widths as our observations of NGC 3256 and performing cloud finding again. An exploration of this type will be presented in a following paper on cloud finding in the Antennae galaxy merger.

We performed two-sample Anderson-Darling tests (Scholz & Stephens 1987) between NGC 3256 and each PHANGS-ALMA galaxy for each of the cloud properties in Figure 3. The null hypothesis here is that both the sample from NGC 3256 and the PHANGS-ALMA galaxy come from the same distribution. The radius distributions between NGC 3256 and NGC 628 appear to originate from the same underlying distribution. Eccentricity distributions from NGC 628, 2903, 3521, and 3627 appear consistent with coming from the same underlying distribution as NGC 3256. Lastly, the mass surface density distributions from NGC 3256 and NGC 4826 also appear to come from the same parent distribution. For all other combinations of galaxies and cloud properties, the null hypothesis is rejected at the five per cent level. These properties for all clouds in NGC 3256 (including unresolved clouds) are reported in Tables 4 and 5, and physical implications of these results are discussed in Section 5. We also performed the same Anderson-Darling tests between each pair of PHANGS-ALMA galaxies and found that for most properties the samples appear to come from different underlying distributions. There are some instances where the null hypothesis could not be rejected (most in eccentricity followed by radius), but there is no obvious systematic trend of which galaxy pairs are indistinguishable. While the differences between the underlying distributions of NGC 3256 and the PHANGS-ALMA galaxies are significant, the dissimilarity also between the PHANGS-ALMA galaxies means we cannot yet attribute the differences in NGC 3256 solely to it being a merger.

4.2 Cloud orientations

Since the distribution of estimated cloud eccentricities is heavily skewed to elliptical clouds, we inspected the spatial distribution of the estimated position angles (PAs) to search for signs of cloud alignment. Given the presence of some spiral structure around the northern nucleus and the edge-on orientation of the southern nucleus, it seemed possible that signatures of cloud alignment may exist due to shear or viewing angle. Figure 4 shows the resolved-cloud positions with their FWHM major and minor axes overlaid on an integrated intensity map of NGC 3256 made from the same signal cube as the cloud finding was carried out on.

We checked the entire sample of resolved clouds across NGC 3256 as well as three regions chosen by eye that appeared to potentially contain clouds more aligned than the entire sample. Clouds in the regions chosen by eye are shown in Figure 4 in red, blue, and orange, and the region boundaries are shown with the dashed black lines and shaded regions. Kolmogorov-Smirnov (KS) tests indicated that the distributions of PAs in each of those samples were not distinguishable from a uniform distribution of angles from 0° to 180° (randomly oriented clouds). Likewise, calculating the PA differences between all pairs of clouds within those samples and using KS tests to compare them to a uniform distribution of angles from 0° to 90° again could not rule out the differences being uniformly distributed. Some small but statistically significant differences from uniform distributions were

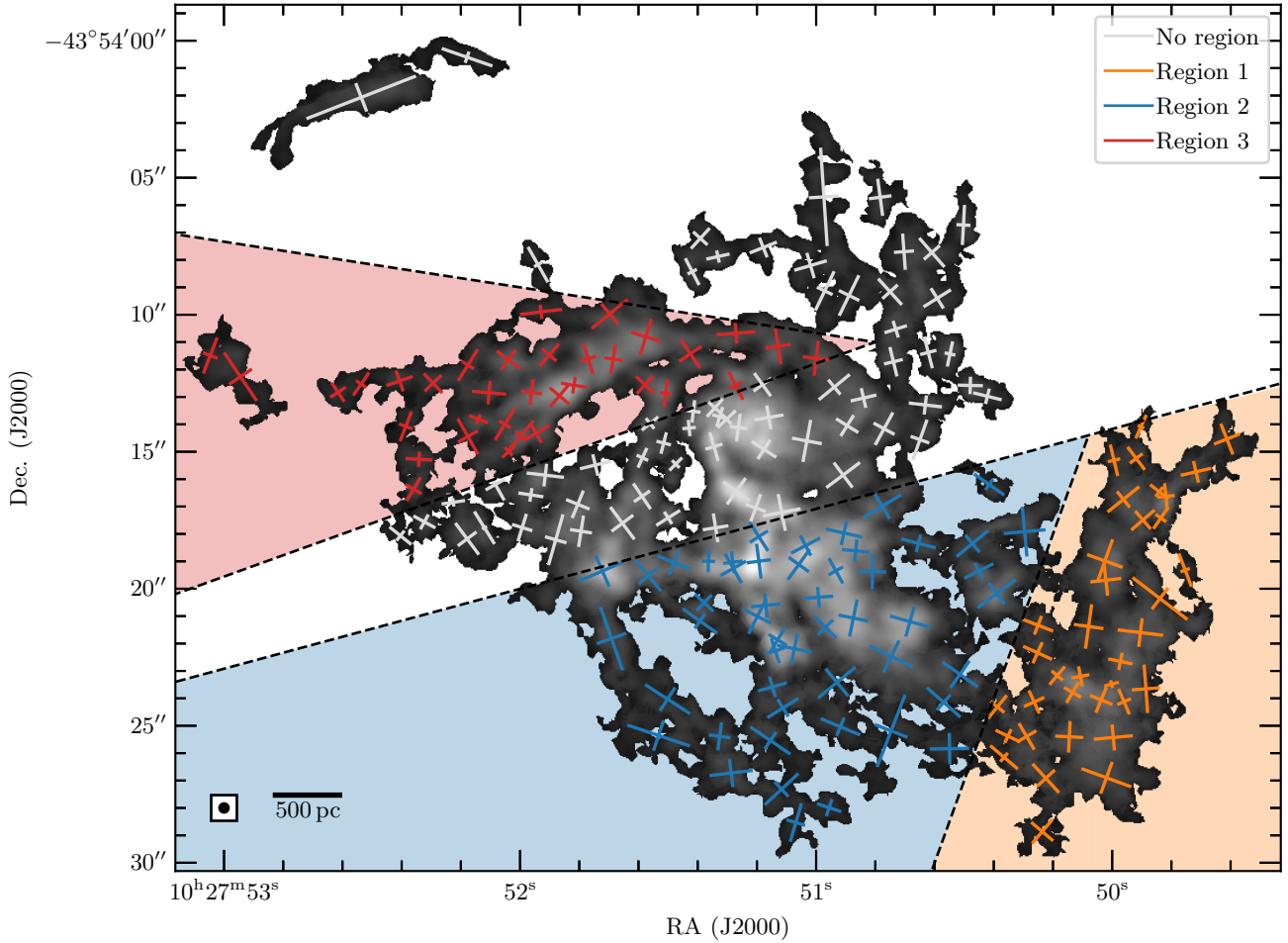


Figure 4. Integrated-intensity map of NGC 3256 calculated from the CO (2–1) cube on which the cloud finding was performed and with the same signal mask as used in cloud finding. Crosses mark the on-sky positions of all resolved clouds, and the length of the bars are equal to the estimated FWHM major and minor axes of the clouds in the plane of the sky. Dashed black lines and colors mark the three regions selected by eye for separate tests of cloud alignment (light-gray crosses were not included in any of these by-eye regions). The circle in the bottom left shows the beam FWHM of 90 pc, and a scale bar is included to show 500 pc at the distance of NGC 3256.

found when binning the PA differences by the separations between the pairs of clouds. However, no clear picture of cloud alignment is revealed since the separation bins were almost all $\gtrsim 1$ kpc. It appears the disturbed morphology of this merger system has prevented any strong signal of cloud alignment being present in these data. However, we hope these results will still be useful for future comparisons to other systems or theoretical studies.

4.3 Cloud mass function

Figure 5 presents the cloud mass function for NGC 3256 in differential form; Figure 6 presents the cumulative mass function. The differential form shows the broad trend of a power law at high masses that turns over at low masses, while the cumulative form reveals some subtle features that are smoothed out in the differential binning. To aid comparison with other studies we fit the cumulative mass function with a double power law of the form

$$N(\geq M) = \begin{cases} AM_{\text{break}}^{(\alpha_{\text{high}} - \alpha_{\text{low}})} M^{(\alpha_{\text{low}} + 1)} & M < M_{\text{break}} \\ AM^{(\alpha_{\text{high}} + 1)} & M \geq M_{\text{break}} \end{cases} \quad (2)$$

where α_{high} is the high mass power law index, α_{low} is the low mass power law index, M_{break} is the mass at which the power law index changes, and A is a normalization constant (Reid & Wilson 2006b). No bounds were applied to any of the free parameters during fitting. We also chose to not apply any corrections to the numbers for completeness because the completeness is not well constrained by the mass alone and to facilitate comparison with the mass function shapes reported by Rosolowsky et al. (2021) who also did not modify the mass-function numbers. Best-fitting parameters are shown in Table 3. Following Reid & Wilson (2006a, see their equation 6 and preceding discussion), the weight on each data point in the individual fits was set to $1/N(\geq M_{\text{CO}})^2$.

Caution should be used when evaluating the quality of the fit by eye, as the logarithmic axes make it difficult to compare how much the fit deviates from the measurements at different masses. Specifically, a visually-large vertical separation in the lower-right appears more significant than the upper-left, though the opposite is usually quantitatively true. Also, the weighting of points is very strong towards the highest masses. For example, the fit being above the measured mass function for the two most-massive clouds contributes the same fraction to the weighted residuals as the fit being below the measure-

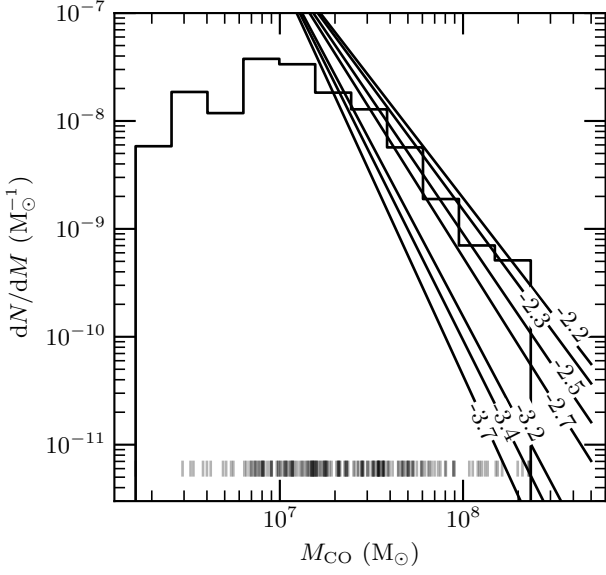


Figure 5. Differential mass function of clouds from NGC 3256 shown by the “step-wise” curve. Unbinned cloud masses are also shown as vertical lines near the bottom. Only resolved clouds are shown for consistency with the remaining figures and subsequent analysis. Straight lines indicate the range of pure power law indices from the PHANGS-ALMA galaxies fit by Rosolowsky et al. (2021).

Table 3. Results of fitting the cumulative cloud mass function with a double power law. Best-fitting parameters come from fitting the measured mass function directly with weights of $1/N(\geq M_{\text{CO}})^2$. The parameter uncertainties were estimated by fitting 10^5 synthetic mass functions derived from the mass uncertainties and finding the 5th, 16th, 84th, and 95th percentiles of the resulting parameter distributions, P_5 through P_{95} . Estimated parameters correspond to those in Equation 2.

Parameter	Best-fitting value	P_5	P_{16}	P_{84}	P_{95}
α_{low}	-1.41	-1.43	-1.42	-1.40	-1.39
α_{high}	-2.75	-2.77	-2.76	-2.70	-2.68
$M_{\text{break}} (10^7 M_{\odot})$	3.06	2.88	2.95	3.11	3.17
$A/10^{15}$	1.1	0.3	0.5	1.2	1.7

ments for the next 12 clouds that are above $10^8 M_{\odot}$. The previous point is partially counteracted by the fact that the density of clouds along the x axis is not uniform (or log uniform; see how the vertical lines at the bottom of Figure 5 are clustered towards the centre of the figure). This concentration of clouds between about 10^7 to $10^8 M_{\odot}$ means that the weights increase more rapidly per dex over that range than they would for a uniform (or log-uniform) distribution of cloud masses. All of this together results in the fitting procedure trying very hard to match the high-mass end, and the extra flexibility around the break mass leading it to landing where the cloud masses are concentrated.

To incorporate the uncertainty on the mass of each cloud in the uncertainties on the best-fitting parameters we used a similar Monte Carlo approach to Reid & Wilson (2006a). We started by generating a new synthetic cloud-mass sample by drawing a random deviate from normal distributions centred at each measured cloud mass and with standard deviations equal to each mass uncertainty. With a new sample of 185 masses we recalculated $N(\geq M_{\text{CO}})$ and fit this synthetic mass function in the same way as the measured masses. We

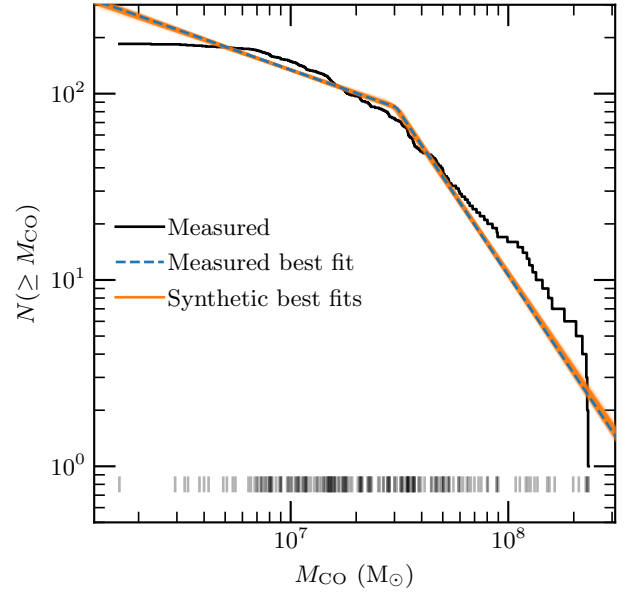


Figure 6. Cumulative mass function of resolved clouds from NGC 3256 shown by the “step-wise” curve. A one-dimensional view of the cloud masses is also shown as vertical lines near the bottom. The dashed blue curve shows the double power law best fit to the measured cloud masses. Orange curves show 200 of the 10^5 best fits to the synthetic cloud mass functions.

carried this out for 10^5 synthetic mass functions and report the inner 68 and 95 per cent of those best-fitting parameters in Table 3.

The uncertainties estimated in this way are likely an underestimate since they are only probing the parameter variations caused by our uncertainties on the masses, with all else held constant. For example, while our choice of initial guess for the fit has little effect on the best-fitting parameters, the initial guess did have some impact on the distributions of the parameters from the synthetic mass-function fitting. The particular initial guess we have used throughout the analysis presented here resulted in symmetric and nearly Gaussian distributions of best-fitting parameters. Further discussion of the mass function, including comparisons to the PHANGS-ALMA galaxies, is in Section 5.5.

4.4 Estimating three-dimensional cloud sizes

Additional properties of the clouds can be derived if the three-dimensional structure of the clouds can be estimated. Rosolowsky et al. (2021) estimate the three-dimensional cloud radius from the geometric mean in each dimension and with an adjustment made for clouds that exceed the characteristic molecular gas disc thickness. They assume a molecular disc FWHM of 100 pc for all galaxies in their sample. With that disc thickness they estimate the three-dimensional cloud radius, R_{3D} , to be either the two-dimensional radius, R , if $R \leq \text{FWHM}/2$ or $\sqrt[3]{R^2 \text{FWHM}/2}$ otherwise. We calculate R_{3D} for the clouds in NGC 3256 in the same way but we use a different molecular disc FWHM that we estimate empirically for NGC 3256 specifically. We take the median of the scale heights for NGC 3256 from Wilson et al. (2019), H_W , and calculate the median molecular disc FWHM = $2\sqrt{\ln 2} H_W \approx 280$ pc.

We calculate the three-dimensional radii for all of our clouds, shown in comparison with the PHANGS-ALMA clouds in Figure 7. Horizontal lines, from bottom to top, show the beam HWHM, the

PHANGS-ALMA molecular disc HWHM of 50 pc, and the disc HWHM for NGC 3256 of ≈ 140 pc. Since the piece-wise form of R_{3D} acts most strongly on the clouds with the largest R , and all of the PHANGS-ALMA clouds are limited by the same disc thickness, the difference between the NGC 3256 and PHANGS-ALMA distributions is more pronounced in R_{3D} than R . Only about seven per cent of the resolved clouds in NGC 3256 have $R \neq R_{3D}$ while this is true for 78 per cent of resolved PHANGS-ALMA clouds.

4.5 Three-dimensional model of clouds

With an estimate for the three-dimensional radius of the NGC 3256 clouds we calculated several additional properties (in combination with the directly-observable properties from Section 4.1) and compare the distributions from NGC 3256 to PHANGS-ALMA in Figure 8. Again, NGC 3256 clouds appear at or above the upper limits of clouds found by [Rosolowsky et al. \(2021\)](#) for most of these quantities (virial mass, size-linewidth coefficient, and internal pressure). However, the virial parameters for clouds in NGC 3256 are similar to the PHANGS-ALMA galaxies. Also, clouds in NGC 3256 have some of the shortest estimated free-fall times, with only NGC 4826 exhibiting shorter free-fall times.

We again performed two-sample Anderson-Darling tests for the properties presented in this section to test if the samples from NGC 3256 and each PHANGS-ALMA galaxy appear to be drawn from the same underlying distribution. The null hypothesis that the samples come from the same distribution was rejected at the 5 per cent level for all galaxies and properties except the virial parameters, size-linewidth coefficients, and internal pressures from NGC 4826. As with the two-dimensional cloud properties however, the same tests between PHANGS-ALMA galaxies also indicated that most samples come from different underlying distributions. These properties for all clouds in NGC 3256 (including unresolved clouds) are reported in Tables 4 and 5, and discussion of possible physical interpretations of these results is in Section 5.

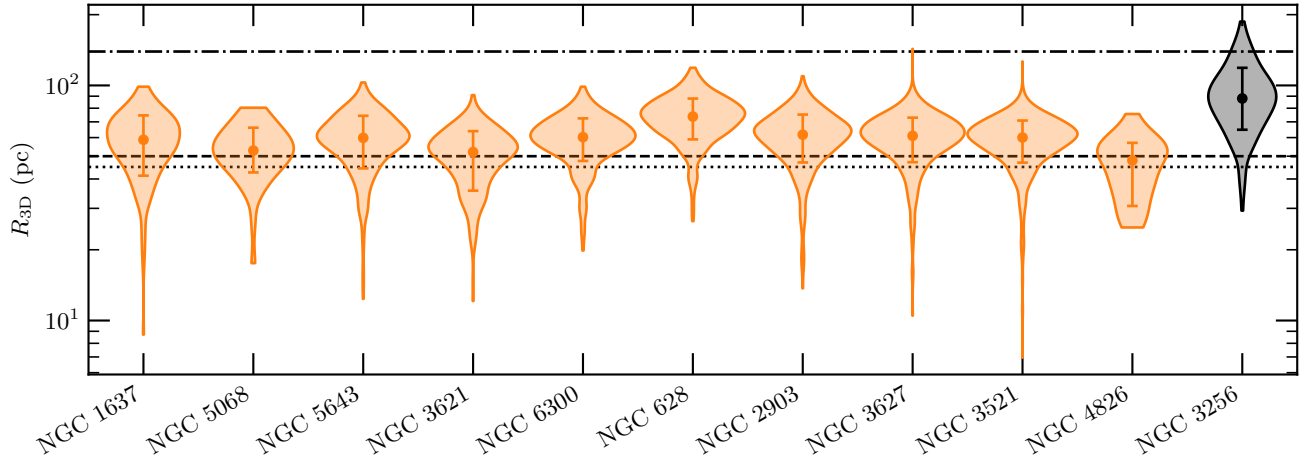


Figure 7. Same as Figure 3 but for estimated three-dimensional radii. Horizontal lines are, from bottom to top, the beam HWHM, molecular disc HWHM of 50 pc used for PHANGS-ALMA galaxies, and disc HWHM of 140 pc for NGC 3256.

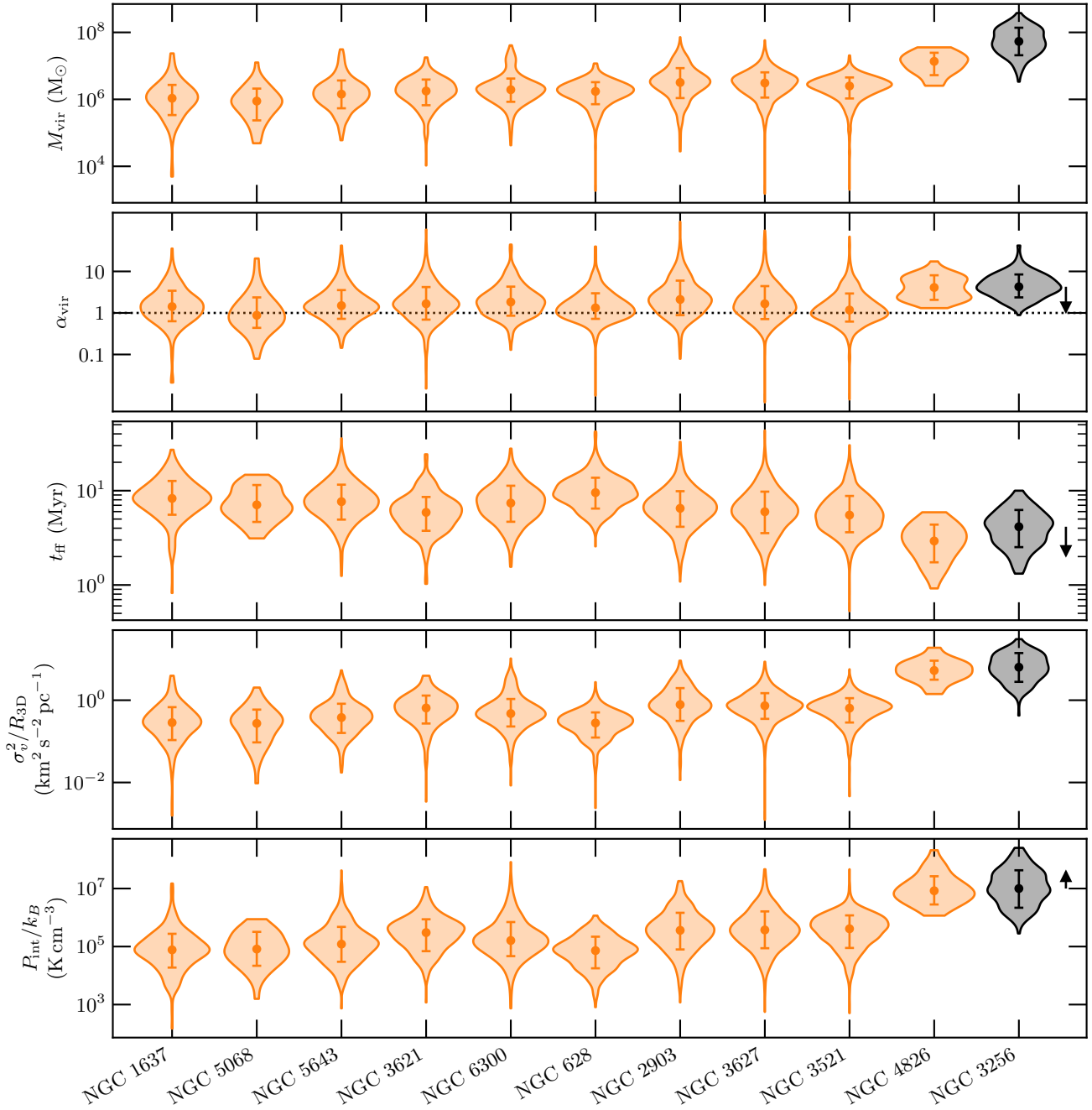


Figure 8. Same as Figure 3 but for properties derived using the three-dimensional radius estimates. The horizontal dotted line at $\alpha_{\text{vir}} = 1$ indicates gravitational virial equilibrium. Calculations of the virial parameter, free-fall time, and internal pressures all depend on the choice of conversion factor. A U/LIRG conversion factor of $1.38 M_{\odot} \text{pc}^{-2} (\text{K km s}^{-1})^{-1}$ is used for NGC 3256. Horizontal arrows again show how the distributions from NGC 3256 that depend on the conversion factor would change if we switched to the Milky Way value. Quantitatively, to change to a Milky Way conversion factor would require dividing the virial parameters by ~ 4.5 , dividing the free-fall times by ~ 2 , and multiplying the pressures by ~ 4.5 .

Table 4. Example of cloud-property table showing the first ten rows and first 17 columns for the clouds found in NGC 3256 with PYCPROPS. The full version is available online in the Supporting Information.

Number	$T_{B,max}$ (K)	$(S/N)_{max}^a$	N_{pix}	R.A. (°; J2000)	Dec. (°; J2000)	v (km s ⁻¹)	σ_v (km s ⁻¹)	$\delta\sigma_v^b$ (km s ⁻¹)	$\sigma_{maj,d}$ (pc)	$\delta\sigma_{maj,d}^b$ (pc)	$\sigma_{min,d}$ (pc)	$\delta\sigma_{min,d}^b$ (pc)	P.A. (°)	e	R (pc)	R_{3D}^c (pc)
1	7.9	8.6	17744	156.9706	-43.9034	2871	11.8	0.7	182	8	79	4	124	0.90	142	141
2	5.2	5.8	8507	156.9710	-43.9032	2872	16.2	0.9	117	9	43	4	69	0.93	83	83
3	9.0	10.0	48931	156.9689	-43.9006	2847	16.7	0.4	378	12	90	4	21	0.97	217	187
4	6.8	7.9	5548	156.9674	-43.9002	2825	5.8	0.5	166	14	28	3	161	0.99	81	81
5	8.0	8.2	10597	156.9616	-43.9016	2720	14.7	1.3	113	8	64	7	98	0.82	100	100
6	11.7	12.5	18584	156.9624	-43.9059	2740	33.4	1.8	92	4	61	4	135	0.75	88	88
7	10.8	11.8	17945	156.9665	-43.9036	2881	24.7	1.5	75	4	58	3	83	0.64	78	78
8	7.4	8.5	6381	156.9584	-43.9055	2660	15.9	1.9	93	9	92	11	97	0.16	109	109
9	6.1	6.2	13402	156.9594	-43.9067	2723	33.9	2.6	72	4	63	3	114	0.50	80	80
10	8.7	9.5	6829	156.9643	-43.9039	2788	23.2	1.5	43	4	34	3	96	0.62	45	45

^a Maximum signal-to-noise ratio over all signal and noise-cube pixels within each cloud.

^b Uncertainties were estimated by PYCPROPS through bootstrapping by resampling, with replacement, the pixels within each cloud 100 times, recalculating the cloud properties for each of those samples of pixels, and calculating the standard error on the mean of each property estimated from those samples. The relative uncertainties produced by PYCPROPS were converted to absolute uncertainties for this table.

^c Calculated from the R column combined with the molecular disc scale height of NGC 3256 estimated by Wilson et al. (2019). See Section 4.4 for details.

Table 5. Continuation of the example cloud-property table for the first ten rows and the last nine columns. The cloud number is repeated as the left-most column for clarity. The full version is available online in the Supporting Information.

Number	L_{CO} (10 ⁶ K km s ⁻¹ pc ²)	δL_{CO}^a (10 ⁶ K km s ⁻¹ pc ²)	M_{CO} (10 ⁶ M _⊙)	Σ_{mol} (M _⊙ pc ⁻²)	M_{vir}^c (10 ⁶ M _⊙)	α_{vir}^c	t_{ff}^c (Myr)	P_{int}/k_B^c (10 ⁶ K cm ⁻³)	P_{comp}^d
1	15.1	0.8	20.8	165	22.6	2.2	9	0.6	0.40
2	6.0	...	8.2	190	25.2	6.1	6	2.2	0.07
3	46.8	1.3	64.5	219	60.7	1.9	7	1.6	0.77
4	5.4	0.5	7.4	180	3.2	0.9	6	0.3	0.60
5	8.8	0.6	12.1	191	25.2	4.2	7	1.5	0.16
6	24.9	1.3	34.3	705	114.0	6.6	3	32.8	0.64
7	28.3	1.2	39.0	1032	55.2	2.8	3	29.9	0.94
8	5.6	0.4	7.7	103	31.8	8.3	10	0.9	0.01
9	11.6	0.5	16.0	404	106.0	13.2	4	21.4	0.11
10	7.6	0.6	10.5	825	28.1	5.4	2	36.4	0.56

^a Uncertainties were calculated the same as described in Table 4.

^b Blank values indicate the value “Not A Number” was the result from PYCPROPS.

^c Calculated using the R_{3D} column.

^d Completeness probability estimated with the logistic-function fit to the completeness results using the M_{CO} , Σ_{mol} , and α_{vir} columns. See Section 3.2 for details.

As the differences between the two-dimensional cloud properties in NGC 3256 and PHANGS-ALMA galaxies appear real with the data available at present, we believe the differences in these properties estimated from the three-dimensional cloud model are also significant. While it is unknown exactly how the emission would be segmented in NGC 3256 if more sensitive observations were obtained, we know that the high peak brightness temperatures and total luminosity in clouds would remain. It is clear that the molecular clouds in NGC 3256 are extreme in their linear sizes, velocity dispersions, and masses which translates to likely harbouring large size-linewidth coefficients and internal pressures. A clear picture on the dynamics of the gas is not possible with these observations alone, as the combination of a high SFR with short free-fall times but also a higher but narrower distribution of virial parameters emphasize the need for a more complete accounting of confining gravitational components that include external forces [Sun et al. \(e.g. 2020a\)](#).

4.6 Correlations between cloud properties

In this section we plot several cloud properties against one another and compare any scaling relations found for clouds in NGC 3256 to PHANGS-ALMA. Generally, clouds found in NGC 3256 appear separated in these parameter spaces from the PHANGS-ALMA population of clouds. In Figures 9 through 12, individual clouds are shown as circles for NGC 3256 and contours indicate the PHANGS-ALMA clouds, estimated from two-dimensional Gaussian KDEs. Using the fit to the completeness results and the `pycprobs`-estimated cloud mass, surface density, and virial parameter we predict the completeness for each cloud and show it as the colour of the circle. The directions of trends in completeness are generally the same between NGC 3256 and the PHANGS-ALMA galaxies. Two additional versions of these scaling-relation plots are shown in Appendix B. One version shows the NGC 3256 clouds coloured by their distance from the nuclei, and the other highlights the NGC 3256 clouds with the smallest radii or lowest velocity dispersions to show where these clouds appear in the different parameter spaces. It is important to keep in mind how a change in the adopted conversion factor would change the results shown here, e.g. switching the NGC 3256 points to the Milky Way conversion factor would move them ~ 0.6 dex higher in CO-estimated mass or mass surface density.

Figure 9 shows cloud velocity dispersions vs. estimated three-dimensional radii. The orange-dashed line shows the fit to Milky Way clouds identified by [Solomon et al. \(1987\)](#). Like the size-linewidth coefficients and internal pressures shown in Figure 8, this figure shows how the velocity dispersions measured in clouds within NGC 3256 exceed expectations from spiral galaxies, even given their larger sizes. Given the limited dynamic range covered in this parameter space relative to the scatter of the data, it is not possible to say if the clouds from NGC 3256 are forming a separate trend that is somehow offset and/or rotated relative to the Milky Way relation. Even despite the large number of clouds identified by PHANGS-ALMA, their distribution of clouds does not show obvious evidence of a trend. [Rosolowsky et al. \(2021\)](#) separate individual galaxies and then bin measurements by radius, which may indicate trends within galaxies that are offset between galaxies, but the significant scatter makes trends within galaxies hard to pin down.

[Hughes et al. \(2013\)](#) caution that trends within the size-linewidth space should be carefully inspected for spatial and spectral resolution origins. Given our matched spatial resolution with PHANGS-ALMA it appears real that the clouds in NGC 3256 are slightly larger. While our spectral resolutions are different by a factor of two, the difference between the median velocity dispersion and the channel width in

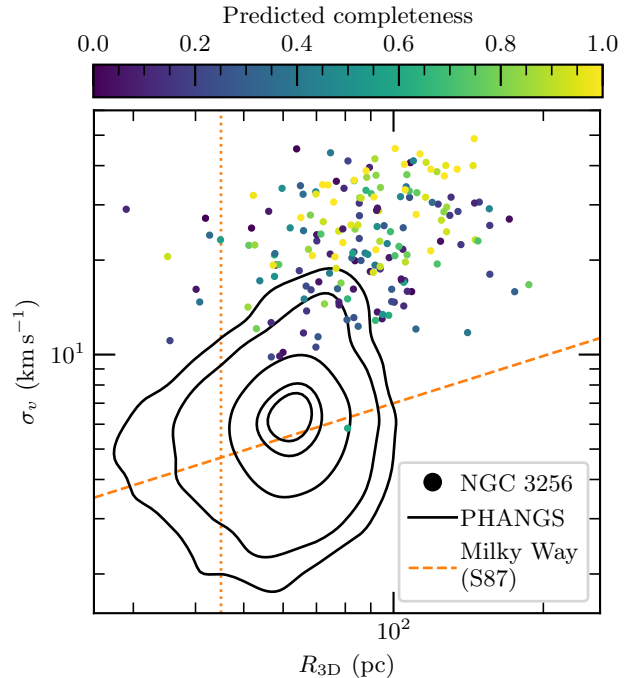


Figure 9. Velocity dispersion vs. three-dimensional radius. Each circle is a resolved cloud from NGC 3256, and black contours enclose 90, 80, 50, 20, and 10 per cent of the resolved PHANGS-ALMA clouds, determined by a Gaussian KDE with uniform weights for all clouds. Cloud circles from NGC 3256 are coloured by predicted completeness from the fit to the completeness test results and the cloud’s estimated mass, surface density, and virial parameter. The orange-dashed line shows the fit to Milky Way clouds from [Solomon et al. \(1987\)](#). The vertical-dotted line shows the beam HWHM of 45 pc.

PHANGS-ALMA is only about two while it is greater than a factor of four in NGC 3256. The higher velocity dispersions in NGC 3256 cannot be explained just by the wider channels.

Figure 10 shows the CO-estimated masses vs. the two-dimensional estimated radii. The orange-dashed lines show trends of constant mass surface density, with the PHANGS-ALMA distribution being centred on $100 M_{\odot} \text{pc}^{-2}$ and most of the clouds from NGC 3256 centred on $300 M_{\odot} \text{pc}^{-2}$. The highest-mass clouds in NGC 3256 actually scatter around mass surface densities of $1000 M_{\odot} \text{pc}^{-2}$, but at the same radii there are also clouds down around $300 M_{\odot} \text{pc}^{-2}$ making the NGC 3256 trend appear to fork at the largest radii. The sparseness of clouds at these most extreme masses and sizes makes it difficult to tell if this split in the trend is real, especially given the strong dependence of the completeness at constant radius but varying mass.

The size-linewidth coefficients vs. mass surface densities are shown in Figure 11. The orange-dashed line indicates where clouds in virial equilibrium would lie without considering external pressure confinement, with both the PHANGS-ALMA and NGC 3256 distributions clearly offset from that line (with the offset being greater for NGC 3256). The curving dotted-orange lines show where clouds in virial equilibrium within a constant external pressure environment would appear ([Field et al. 2011](#)). Generally higher pressures are needed for the NGC 3256 clouds to be kept in virial equilibrium. The external pressure confined picture from Figure 11 is important to consider when interpreting the distributions of virial parameters in clouds from NGC 3256 in Figure 8, since external pressure is not included in the calculation of α_{vir} . The clouds in NGC 3256 may

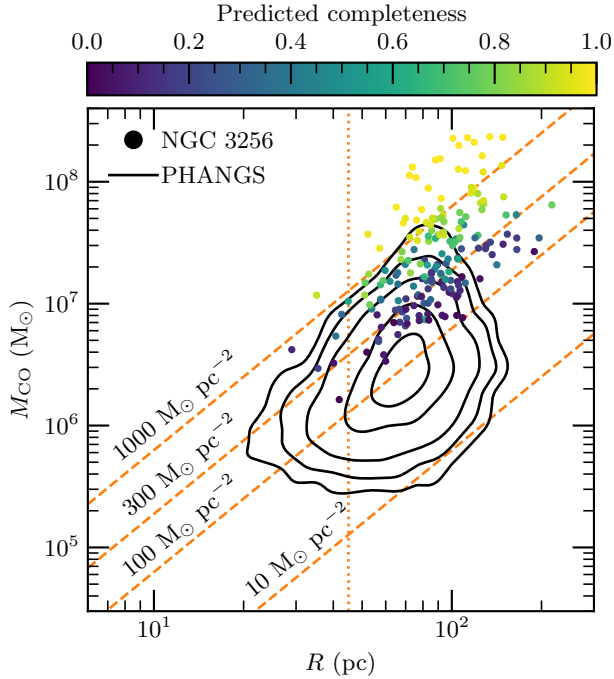


Figure 10. CO-estimated cloud mass vs. two-dimensional radius. Symbols are the same as in Figure 9, but contours here enclose 95, 90, 80, 50, and 20 per cent of the PHANGS-ALMA clouds. The orange-dashed lines indicate constant mass surface densities. The vertical-dotted line shows the beam HWHM of 45 pc. A U/LIRG conversion factor of $1.38 M_{\odot} \text{pc}^{-2} (\text{K km s}^{-1})^{-1}$ was used to calculate the CO masses in NGC 3256; changing to the Milky Way conversion factor would shift those points up by ~ 0.6 dex.

appear far from virial equilibrium, with far too much kinetic energy; however with sufficient confining pressure they could be held together and even made to collapse.

The relation between virial mass and CO-estimated mass is shown in Figure 12. Both PHANGS-ALMA and NGC 3256 clouds are shifted to higher virial masses than expected for virial equilibrium, but the significantly higher velocity dispersions in NGC 3256 mean its clouds are shifted further. Similar considerations around the presence of significant external pressure in NGC 3256 described for the size-linewidth coefficients should be kept in mind when interpreting the virial masses.

5 DISCUSSION

5.1 Cloud properties that differ between NGC 3256 and PHANGS-ALMA

In Figure 3, the velocity dispersions of the clouds found in NGC 3256 stand out as most dissimilar to the clouds found in the PHANGS-ALMA sample by Rosolowsky et al. (2021). Figure 5 from Rosolowsky et al. (2021) shows clouds from the centres of galaxies have consistently the highest velocity dispersions, overlapping with the low end of the NGC 3256 distribution. In a pixel-based analysis, Brunetti et al. (2021) found that the centres of PHANGS-ALMA galaxies were most similar to the non-nuclear regions in NGC 3256. The magnitude of the velocity dispersions measured across (most) of the PHANGS-ALMA sample are expected to originate primarily from star-formation driven turbulence (Shetty & Ostriker 2012;

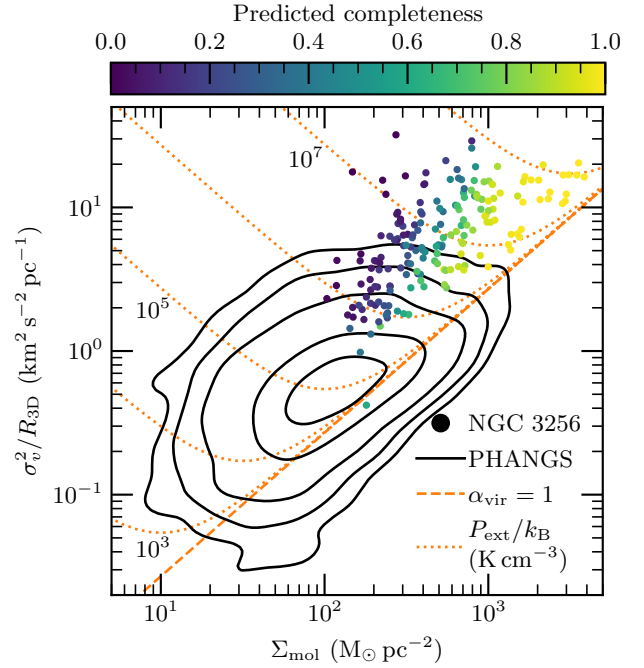


Figure 11. Size-linewidth coefficient vs. mass surface density. Symbols and contours are the same as in Figure 10. The orange-dashed line shows where clouds in virial equilibrium ($\alpha_{\text{vir}} = 1$) would lie with no external pressure. Orange curving-dotted lines show where clouds would lie in virial equilibrium if instead they do experience external pressures, in units of $\text{K cm}^{-3} k_{\text{B}}^{-1}$. A U/LIRG conversion factor of $1.38 M_{\odot} \text{pc}^{-2} (\text{K km s}^{-1})^{-1}$ was used to calculate the mass surface densities in NGC 3256, and changing to the Milky Way conversion factor would shift those points to the right by ~ 0.6 dex.

Krumholz et al. 2018). However, to reach the velocity dispersions measured in NGC 3256, Krumholz et al. (2018) suggest gas flows into the centres of galaxies are also needed. Interaction-induced torques drive the gas to flow towards the centres of merging systems (Noguchi 1988; Mihos & Hernquist 1996; Iono et al. 2004) which, in the model by Krumholz et al. (2018), likely explains the enhanced velocity dispersions in NGC 3256.

Gas flows driven by interactions may also explain the high velocity dispersions in NGC 4826, since it is thought to have undergone a merger in the past that drove most of the ISM into the centre of the galaxy (Braun et al. 1994). To a lesser extent this may also explain NGC 3627 having the third highest median velocity dispersion in the PHANGS-ALMA sample due to its likely interaction with NGC 3628 (Rots 1978; Soida et al. 2001).

It is interesting that most clouds in NGC 3256 appear with significantly larger velocity dispersions and many with slightly larger radii, compared to PHANGS-ALMA clouds. In a similar comparison at matched resolution (~ 53 pc with 5 km s^{-1} wide channels) and sensitivity, Hughes et al. (2013) found that clouds in the interacting NGC 5194 system have a distribution of radii very similar to NGC 598 and the Large Magellanic Cloud but elevated velocity dispersions. They observed that the regions of NGC 5194 that harboured higher velocity dispersions were also where the SFR was lower. They argued that non-transient clouds are likely to be in a state that balances their internal turbulence with external pressure as well as gravity (satisfying $\sigma_v \propto P_{\text{ext}}^{1/4} R^{1/2}$). They concluded that the elevated velocity dispersions at the same cloud sizes were driven more by differing

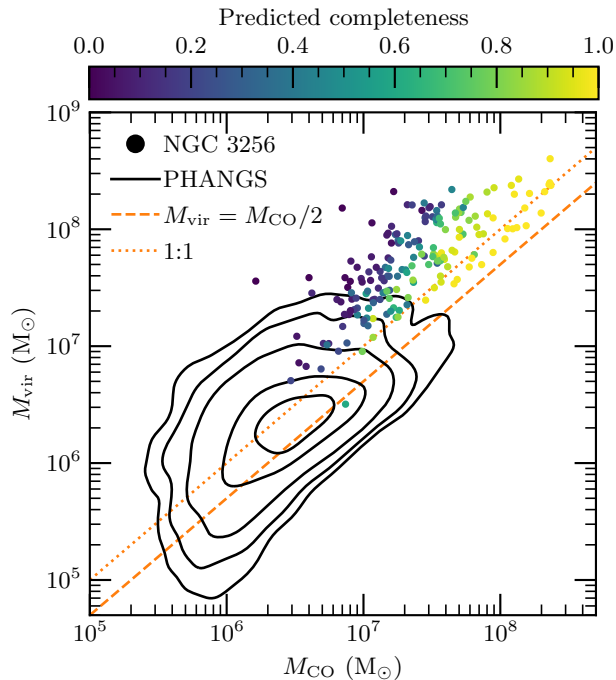


Figure 12. Virial mass vs. CO-estimated mass. Symbols and contours are the same as in Figure 10. The orange-dotted line shows where the virial mass is equal to the luminous mass and the dashed line shows where the virial mass is equal to half the luminous mass. The latter is expected for clouds in virial equilibrium when using two-dimensional Gaussian profiles for clouds, following Rosolowsky et al. (2021). A U/LIRG conversion factor of $1.38 M_{\odot} \text{pc}^{-2} (\text{K km s}^{-1})^{-1}$ was used to calculate the CO masses in NGC 3256, and changing to the Milky Way conversion factor would shift those points to the right by ~ 0.6 dex.

external pressures between galaxies rather than different amounts of star-formation driven internal turbulence. However, in NGC 3256 we find a mix with clouds having both similar and larger radii to PHANGS-ALMA while almost always having larger velocity dispersions. In NGC 3256, enhanced external pressures alone could not simultaneously increase the velocity dispersions and radii, so there are likely additional sources of turbulence in NGC 3256 relative to PHANGS-ALMA.

If the external pressures were similar between NGC 3256 and PHANGS-ALMA and Larson’s size-linewidth relation held, then increased velocity dispersions would result in larger radii that lie along the dashed line in Figure 9. The vertical offset of the clouds in NGC 3256 from the dashed line to higher velocity dispersions may then indicate higher external pressures in NGC 3256. Shown another way, clouds from NGC 3256 are offset to higher internal pressures relative to PHANGS-ALMA in Figure 8. If the clouds are non-transient objects then the external pressures would have to be higher just to keep them bound, let alone collapse to form stars.

It is also interesting to qualitatively compare the integrated-intensity maps of NGC 3256 (figure 1 from Brunetti et al. 2021) and NGC 4826 (figure 6 of the supplementary material from Rosolowsky et al. 2021) because both galaxies exhibit smoother emission across the FoV compared to the much more clumpy appearance of the rest of the PHANGS-ALMA maps. However, the FoV mapped in NGC 4826 only reaches a radius of about 1 kpc, the same radius used to define the central regions of PHANGS-ALMA galaxies by Sun et al. (2018). Thus, the clouds from NGC 4826 come solely from the central por-

tion of the galaxy which Brunetti et al. (2021) found was the part of PHANGS-ALMA galaxies most similar to NGC 3256.

The CO luminosities of the clouds in NGC 3256 are also significantly larger than those in the PHANGS-ALMA galaxies, even compared to NGC 4826. Brunetti et al. (2021) found pixel-based peak brightness temperatures in NGC 3256 reaching up to 37 K (similar to those we find within clouds shown in Table 6 and Figure 13) compared to 15 K in PHANGS-ALMA galaxies (Sun et al. 2018, 2020b). Combined with the large velocity dispersions in NGC 3256, it is not surprising the CO luminosities are extreme as well (Bolatto et al. 2013). From these luminosities, cloud masses are estimated to be significantly larger than in the PHANGS-ALMA sample, despite using a U/LIRG conversion factor that is between 3 and 11 times smaller than the values used by Rosolowsky et al. (2021). While the largest masses may originate from clouds blended in space and velocity near the nuclei, giant molecular clouds (GMCs) of masses $\sim 10^8 M_{\odot}$ are likely necessary to produce star clusters with masses similar to globular-cluster progenitors (Howard et al. 2017). Adamo et al. (2020) measured the upper-mass cutoff to the cluster mass function in NGC 3256 to be among the highest in local galaxies, which is consistent with this prediction of massive clouds resulting in the formation of massive star clusters.

Combining these mass estimates with the fairly similar cloud sizes seen in NGC 3256 and PHANGS-ALMA, we see the molecular gas mass surface densities in NGC 3256 exceed those measured in PHANGS-ALMA galaxies. Kruijssen (2012) predicts a correlation between the mass surface density of molecular gas and the cluster-formation efficiency (CFE). Adamo et al. (2020) find general agreement between this theoretical prediction and their observations of nearby mergers as well as nearby spiral galaxies from the literature. Specifically, Adamo et al. (2020) estimate an upper limit on the CFE in NGC 3256 that is higher than most local galaxies. If the surface density-CFE correlation prediction by Kruijssen (2012) holds in general, then the extreme molecular gas mass surface densities in NGC 3256 relative to the PHANGS-ALMA galaxies would imply its CFE is high relative to the PHANGS-ALMA sample as well.

Virial mass comparisons are very similar to those for velocity dispersion, given the strong dependence of virial mass on the velocity dispersion of the cloud. Interestingly, the virial-mass distribution from NGC 3256 is one of the widest shown in Figure 8, potentially exhibiting blended double peaks. However, when the virial masses are combined with the CO masses to estimate the virial parameter, the resulting distribution from NGC 3256 is one of the narrowest. This implies most of the clouds in NGC 3256 have their mass closely tracking with their size and velocity dispersion so that a relatively narrow range of dynamical states are present, compared to some of the distributions of clouds found in the PHANGS-ALMA galaxies.

NGC 4826 has virial masses more closely approaching NGC 3256 than the other galaxies. The two galaxies have a similar median virial parameter, but NGC 4826 exhibits a different interplay between virial mass and virial parameter. Although there is a hint of a multi-modal distribution of virial masses in NGC 4826 with a peak clearly around $1.5 \times 10^7 M_{\odot}$ and a possible second peak near $3 \times 10^6 M_{\odot}$, it is clearly multi-modal in virial parameter. The lower virial-parameter peak in NGC 4826 around 2 could indicate collapsing or marginally unbound gas while the second peak near 7 is either very unbound or requires a significant external-pressure contribution to remain bound. Given the relatively broad distributions of the other virial-parameter distributions from the PHANGS-ALMA galaxies (which can be seen by comparing the widths of the violins in Figure 8), perhaps we are seeing evidence that the ISM in these local spiral galaxies contains gas in a wider variety of dynamical states than the gas in NGC 3256.

The internal turbulent pressures in NGC 3256 not only appear significantly higher than PHANGS-ALMA (except NGC 4826) but also exhibit the widest distribution with about three blended but distinct peaks. If we assume most of the molecular gas is near pressure equilibrium, as Sun et al. (2020a) found with a subset of the PHANGS-ALMA sample, then this would imply there is also a wider range of external pressures present in NGC 3256 than the nearby spiral galaxies. For example, the violent rearrangement of gas through the merger process with significant mass inflow towards the nuclei could enhance external pressures. At the same time, gas in the outskirts of the progenitors of NGC 3256 would likely be less perturbed. It is intriguing that NGC 3256 has one of the narrowest distributions of virial parameter since the merger-driven rearrangement of the gas should also impact the state of the gas within clouds. Processes seem to be conspiring to take the morphological mess that has been made of the gas and make its dynamics conform to a smaller range of states.

5.2 Cloud properties that are similar between NGC 3256 and PHANGS-ALMA

The cloud radii are one of the more consistent quantities between NGC 3256 and PHANGS-ALMA galaxies. Given the matched resolution of all the observations, and the tendency of algorithms like PYCPROPS to identify structures near the resolution limit of the data, it is not too surprising how similar the distributions of radii between these galaxies are. On the other hand, NGC 3256 has the second largest median radius (second to NGC 628) and about 25 per cent of its clouds have radii exceeding most of the rest of the PHANGS-ALMA galaxies. While PYCPROPS attempts to remove observational effects in most of its estimates of cloud properties, our tests of the accuracy of the radius estimates (albeit without the effects of source blending; see Section 3.2) indicated it was systematically underestimating the true radii by about 30 per cent, meaning the true distribution of cloud radii may be shifted to even larger values. Rosolowsky et al. (2021) do not find a systematic bias in the estimates of the radii in the PHANGS-ALMA data, so a similar shift to the true cloud radii is not expected for the PHANGS-ALMA distributions. Finally, the higher noise level in our observations of NGC 3256 would likely truncate the full spatial extent of clouds since S/N cuts are used to select significant emission. Better sensitivity would lead to more of the FoV being filled with significant emission, but it is ultimately difficult to predict how this would affect the radius distribution because PYCPROPS would likely still be identifying sources near the beam size.

Dobbs et al. (2011) presented a connection between the aspect ratios of simulated clouds and their estimated degree of binding by self-gravity. They found that their populations of simulated clouds with lower virial parameters appeared more spherical and regularly shaped than populations with elevated virial parameters in simulations with greater levels of stellar feedback. Additionally, their simulations which best matched observed distributions of virial parameters in Galactic clouds also matched the observed distribution of Galactic cloud aspect ratios (with the majority between 1.5 to 2; e.g. Koda et al. 2006). Dobbs et al. (2011) gave an example of a long-lived and massive cloud which at first appeared fairly filamentary when its virial parameter was highest. At later times, it appeared much more round and its virial parameter had dropped by a factor of about three. In the observations presented here, we argue that the meaningful point to take away is that the molecular structures found in NGC 3256 appear slightly larger than PHANGS-ALMA but the distributions of shapes are indistinguishable. This may indicate that the enhanced velocity dispersions act to “puff up” the clouds in NGC 3256 but on average their dynamical state is similar to clouds

in nearby spiral galaxies. It is important to note that at any instant an individual cloud’s aspect ratio will not necessarily predict whether it will remain bound, but with a reasonable cloud sample size it may be possible to say if the size scale being probed is the primary size of objects that are bound.

5.3 Free-fall times

A noteworthy feature of the free-fall times in NGC 3256 is that they are actually not as different as might be expected given the higher surface densities compared to the PHANGS-ALMA galaxies. Since the free-fall time is proportional to the inverse of the volume density it appears the slightly larger cloud radii overcome some of the differences in mass so that the distributions of free-fall times overlap considerably.

Wilson et al. (2019) estimated free-fall times ranging from 2.5 to 14 Myr in NGC 3256 at 512 pc resolution. Despite our linear resolution being almost 6 times smaller than those observations (or 32 times smaller in area) we estimate free-fall times ranging from 1 to 10 Myr. These similar free-fall times would imply similar average molecular gas volume densities between 90 and 512 pc scales. Fairly constant gas properties across these size scales is also consistent with the minimal changes in pixel-based estimates of molecular gas surface density, velocity dispersion, and peak brightness temperature found by Brunetti et al. (2021) in NGC 3256 at scales from 55 to 120 pc. The interpretation that the molecular ISM in NGC 3256 may be relatively smooth on the scales analysed by Brunetti et al. (2021) may also extend up to scales of about 500 pc, since otherwise differing filling factors would result in measured gas densities changing with resolution. For example, Sun et al. (2018) find more significant trends in these properties in their pixel-based analysis of PHANGS-ALMA galaxies at scales from 45 to 120 pc, indicative of the clumpy nature of the ISM in nearby spiral galaxies.

The efficiency per free-fall time is set by the ratio of the free-fall time to the gas depletion time ($\epsilon_{\text{ff}} \equiv t_{\text{ff}}/t_{\text{dep}}$ where $t_{\text{dep}} = \Sigma_{\text{mol}}/\Sigma_{\text{SFR}}$). While the distribution of free-fall times in NGC 3256 reaches much smaller values than most of the PHANGS-ALMA clouds from Rosolowsky et al. (2021), about half the distribution overlaps with most of the PHANGS-ALMA free-fall times. It seems that it is the difference in depletion times between NGC 3256 and the PHANGS-ALMA galaxies that plays the dominant role in producing values of ϵ_{ff} that are almost an order of magnitude larger in NGC 3256 compared to spiral discs at 500 pc scales (Wilson et al. 2019).

The question of how the molecular-gas depletion times in NGC 3256 compare at cloud scales to previous observations around 500 pc remains open. While the molecular mass surface densities measured here at 90 pc resolution are comparable to those at 512 pc resolution (Wilson et al. 2019), measurements of the SFR surface density at 90 pc resolution are lacking. In principle, continuum measurements from the observations presented here could give an estimate of the SFRs in the regions of highest molecular gas surface density. However, continuum measurements using solely these ~ 230 GHz observations will include significant contamination from dust emission. The addition of observations at 100 GHz would help extract just the free-free component for estimating the SFR.

With direct estimates of the free-fall times from this work and depletion times from the continuum, it would be possible to estimate ϵ_{ff} on cloud scales. At 90 pc resolution, it may be that the difference in ϵ_{ff} between U/LIRGs and spirals is not as large as at ~ 500 pc resolution. Unfortunately, a comparison of ϵ_{ff} between spiral galaxies and starbursts on the scale of GMCs is complicated by the stochastic

nature of star formation at those physical scales. However, it does raise the interesting possibility that the degree of stochasticity at a given scale may depend on the absolute level of the SFR in the system. For example, if the SFR surface density were ten times higher in a particular galaxy, then about ten times the number of star-forming sites per unit area would be present. In this situation, the area that would have to be averaged over to fully sample all star-formation stages to obtain an accurate estimate of ϵ_{ff} could be about ten times smaller than in a galaxy with a lower SFR surface density. Imaging the CO and continuum observations at a range of resolutions and recalculating free-fall times, depletion times, and ϵ_{ff} would allow us to explore the scatter in these quantities as a function of physical scale.

5.4 Pixel-based vs. cloud-based emission decomposition

Figure 13 shows that there is general agreement between the cloud-finding results presented here and the pixel-based decomposition of these observations from Brunetti et al. (2021)⁶. This comparison also highlights the complementary nature of these two analyses. The pixel-based method removes the requirement of choosing what conditions indicate boundaries between clouds, and therefore eliminates differences between analyses originating from the chosen definition of a cloud. However, the pixel-based analysis assumes that each beam is filled with roughly one GMC that is the same size as the beam. The cloud-finding analysis identifies relevant physical size scales so that properties like average surface density, mass, virial parameter, and internal pressure can be calculated using sizes determined from the data. Also, the ability of the cloud-finding decomposition to automatically analyse lines of sight made up of multiple spectral components allows us to potentially extract more information from the observations.

To facilitate comparison with Sun et al. (2018), Brunetti et al. (2021) calculated percentiles and Gaussian KDEs of the pixel-based distributions using mass weighting, while Figures 3 through 12 in this paper use uniform weights for all clouds. We compared pixel and cloud distributions with both mass and uniform weighting and found that the comparisons were similar in both cases. Figure 13 shows the mass-weighted Gaussian KDEs comparing several properties of the molecular gas estimated with the pixel and cloud-based methods.

Qualitatively, the distributions of mass surface density and internal pressure are quite consistent between the pixel and cloud-based analyses. Distributions of peak brightness temperatures from the cloud identification peak at higher values than those of the pixel-based analysis, and the clouds reach somewhat higher temperatures. Conversely, velocity dispersion, virial parameter, and free-fall time distributions peak at lower values from the cloud measurements than pixels. Velocity-dispersions measured in clouds are more consistent with pixels that exclude the nuclei (i.e. pixels whose distances from both nuclei are >1 kpc after accounting for the inclination angles of the nuclei). The mass-weighted inner 68th percentiles for distributions from both methods are reported in Table 6.

The fact that the velocity-dispersion distributions from non-nuclear pixels and clouds are so similar despite the western region not

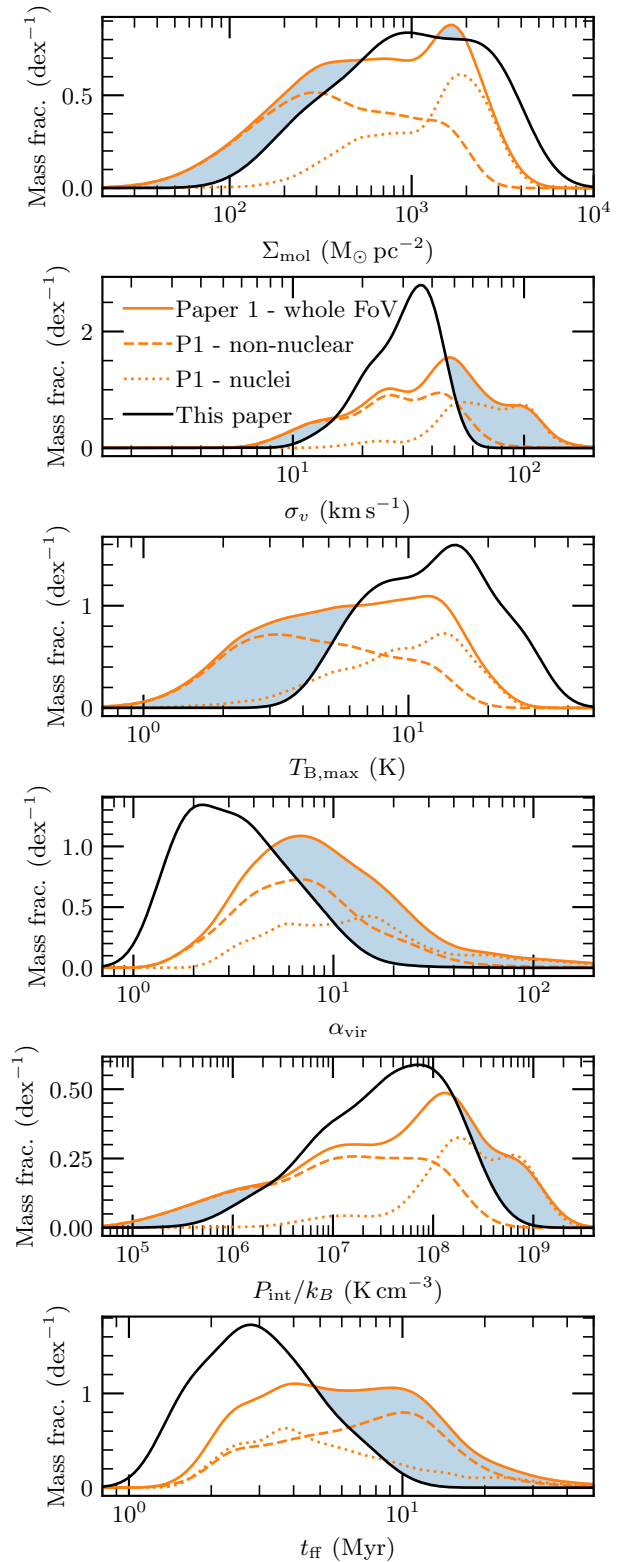


Figure 13. Mass-weighted Gaussian KDEs comparing molecular gas properties measured in clouds at 90 pc resolution (black) to those measured from the pixel-based analysis from Brunetti et al. (2021) at 120 pc resolution (orange). Distributions from the pixel analysis are also broken into the non-nuclear (dashed) and nuclear (dotted) components. Blue-shaded regions show where the pixel distribution is above that from the clouds, to highlight where the distributions are most different. The same U/LIRG CO-to-H₂ conversion factor was used in both analyses.

⁶ To avoid lines of sight with multiple spectral components, Brunetti et al. (2021) excluded pixels west of an R.A. of approximately $10^{\text{h}}27^{\text{m}}50^{\text{s}}.3$. Additionally, two polygonal regions around the jet originating from the southern nucleus were excluded based on enhanced velocity dispersions along linear features extending roughly north-south of the southern disc. These regions have not been excluded from the cloud-finding analysis.

Table 6. Mass-weighted inner 68th percentiles for the cloud and pixel-based distributions.

Quantity (units)	Cloud		Nuclear pixels		Non-nuclear pixels	
	P_{16}	P_{84}	P_{16}	P_{84}	P_{16}	P_{84}
Σ ($M_{\odot} \text{pc}^{-2}$)	360	2800	500	2400	140	1200
σ_v (km s^{-1})	21	40	45	100	14	47
$T_{B,\text{max}}$ (K)	7	20	5	16	2	10
α_{vir}	2	6	5	34	3	15
P_{int}/k_B (10^6K cm^{-3})	7	120	75	720	1	93
t_{ff} (Myr)	2	5	3	11	3	13

being included in the pixel distributions likely indicates the spectral decomposition of clouds was successful at separating components along the line of sight. The multiple spectral components likely arise from independent gas features along the line of sight (e.g. gas from the two progenitor galaxies overlapping in projection) rather than gas with significantly different turbulent motions. The automatic spectral decomposition provided by cloud finding in the full PPV cube is especially useful in morphologically disturbed merger systems where the line of sight can be very complex due to gas overlapping in projection.

While the pixel and cloud distributions are generally consistent, some of the larger differences appear to be related to limitations in the pixel-based analysis. For example, the higher peak brightness temperatures measured in the cloud distribution are mainly found in regions associated with the jet in the cloud analysis that are not in the pixel-based analysis. The higher peak temperatures were excluded from the pixel method to ensure a thorough removal of the jets, but that exclusion could have been too aggressive, allowing the cloud analysis to retain more pixels closer to the jet in spatial projection but spectroscopically distinct from it. Related to the fixed pixel size, the distribution of cloud pressures does not extend as high as estimated in individual pixels. The internal pressure goes as $P_{\text{int}} \propto R^{-1} \Sigma_{\text{mol}} \sigma_v^2$ where R is the pixel size in the pixel-based analysis (Sun et al. 2018) or the three-dimensional radius for clouds (Rosolowsky et al. 2021). Thus, the constant pixel size appears to overestimate the pressures for the largest clouds more than it underestimates it for the smallest clouds. Although some care needs to be taken when comparing the extrema of distributions between the pixel and cloud-based methods, if the beam size is close to the median cloud radius then the bulk of the molecular gas properties appear to agree between the two methods.

5.5 Mass function comparisons

5.5.1 Previous cloud decomposition

The observations presented here have also been independently imaged and analysed through cloud finding with `cPROPTOOL` by Mok et al. (2020). We adjust the masses from Mok et al. (2020) to use our choices of distance to NGC 3256, CO 2–1 to 1–0 ratio, and CO-to-H₂ conversion factor. Unlike in our analysis, Mok et al. (2020) do not convolve the observations, retaining the full resolution they achieve of $95 \times 60 \text{ pc}$ (adjusted from their adopted distance to NGC 3256 of 36 Mpc to 44 Mpc used here) or about 70 per cent the beam area of

our 90 pc FWHM beam. Their noise root-mean-square (RMS) is also likely different than ours, because of the different beam sizes and the addition of noise in our data cube to homogenize the RMS throughout the cube. Despite these differences, they found 123 GMCs above their completeness limit of $1.5 \times 10^7 M_{\odot}$ where we found 120 above that limit (all resolved spatially and spectrally). Their completeness limit mass is also near where our differential and cumulative mass functions both deviate from high-mass power laws. Finally, their maximum cloud mass of $2.9 \times 10^8 M_{\odot}$ is about 20 per cent higher than ours.

To characterize the shape of the GMC mass function in NGC 3256, Mok et al. (2020) fit both a Schechter function and pure power law. The Schechter function results do not place strong constraints on the characteristic cutoff mass and there is not a strong preference for either the Schechter or power law functional form. Mok et al. (2020) report a pure power law index of -2.10 (with a 1σ confidence interval from -2.20 to -2.00), which is almost exactly halfway between our low and high mass indices. Since their low-mass cutoff in fitting the mass function is about a factor of two smaller than our break mass, we would expect their slope to be intermediate between our low and high-mass slopes as it tries to account for some of the curvature in the mass distribution.

Simulated and actual observations of star forming regions analysed at different angular resolutions, with beam-area ranges of about a factor of 100, show very little or no variation in the high-mass slope of source mass functions (Reid et al. 2010; Louvet et al. 2021). Therefore, our mass function may be more consistent with that from Mok et al. (2020) than initially anticipated from the differing resolutions, especially considering how close the beam sizes in these analyses of NGC 3256 are. Less easy to predict is the effect of the differing noise levels between the analyses due to the noise level varying throughout the cube used by Mok et al. (2020). While Reid et al. (2010) generally found that increasing the noise at fixed resolution resulted in somewhat shallower high-mass slopes in their mass-function fits, the noise difference in the two analyses of NGC 3256 depends on where in the cube (position and velocity) each cloud was found. Since most of our clouds were found near the central velocity of the galaxy, where the original noise is worst, it seems reasonable that the resulting mass function slopes would not be wildly different.

5.5.2 PHANGS-ALMA

Rosolowsky et al. (2021) performed similar fits to Mok et al. (2020) on the GMC mass functions from their sample of 10 galaxies, with the addition of attempting to also fit for the effect of completeness causing the turnover at low masses. Four of the mass functions show significant preference for Schechter-function fits over a pure power law (NGC 628, 2903, 3521, and 3627) but the remainder do not show evidence for a preference. The pure power-law indices are shown in Figure 5 as the straight lines overplotted on our differential mass function from NGC 3256, ranging from -2.2 to -3.7 . Our high-mass slope is near the middle of the distribution of slopes from PHANGS-ALMA. It is worth noting that robust comparisons over the same mass range cannot be made between NGC 3256 and the PHANGS-ALMA galaxies due to the majority of our most-complete clouds being at or above the most-massive PHANGS-ALMA clouds.

Some of the same limitations are present in our mass function for NGC 3256 as those from PHANGS-ALMA. Blending of sources in crowded regions due to coarse spatial resolution will alter the measured mass function shape from the true underlying distribution, and this effect is likely worse in NGC 3256 than in the galaxies from PHANGS-ALMA. The result of source blending on the shape

of a mass function can be difficult to predict since small but not necessarily low-mass clouds will be most blended, blending is worst for the higher-mass clouds for which crowding is worst, and low-mass clouds can be artificially formed by the combination of neighbouring noise peaks or low-mass clouds below the detection threshold (Reid et al. 2010). Also, Rosolowsky et al. (2021) note that their estimates of mass completeness indicate they are only able to measure the mass-function shape over a relatively small mass range (a factor of about ten between the lowest and highest robust masses). Our rough estimates of where the mass completeness is significantly impacting the shape of the mass function in NGC 3256 are where the differential mass function begins to turn over ($\sim 10^7 M_{\odot}$) and the double power law break mass ($3 \times 10^7 M_{\odot}$). Thus, we are also limited to a mass range of about a factor of ten where our mass function is most robust.

Again, these comparisons must be made with caution due to the differing noise levels in our observations of NGC 3256 and those from PHANGS-ALMA. A lack of clouds in our sample with similar luminosities or masses to PHANGS-ALMA is predominantly an observational effect, such that the full distribution of clouds in NGC 3256 likely includes low-luminosity or mass PHANGS-ALMA-like clouds. However, it is not straightforward to predict how improved-sensitivity observations of NGC 3256 would alter the cloud distribution. First, we would detect gas down to lower surface densities, which would reveal new low-mass clouds as well as add low surface-density gas to the outer extents of already-identified clouds. Whether this new gas is assigned to new or pre-existing clouds would depend on the S/N contrast of the new emission. The second effect is the tendency for algorithms like PYCPROPS to break emission up into roughly beam-sized structures, so the spatial extent of the new emission would also impact how it was assigned to new or existing clouds. It is clear, though, that a population of clouds on scales of 90 pc in NGC 3256 is significantly more luminous (and likely also more massive) than in the PHANGS-ALMA galaxies.

6 CONCLUSIONS

We have performed molecular-cloud identification on observations of the nearest LIRG, NGC 3256, at a matched resolution of 90 pc to the PHANGS-ALMA cloud-finding results presented by Rosolowsky et al. (2021). In these CO (2–1) observations we have identified 185 spatially as well as spectrally resolved clouds, which in almost all properties analysed are extreme relative to the PHANGS-ALMA sample. Our full catalogue of clouds is provided in Tables 4 and 5.

Cloud velocity dispersions, luminosities, CO-estimated masses, mass surface densities, virial masses, virial parameters, size-linewidth coefficients, and internal turbulent pressures are all significantly higher than values measured in clouds in the PHANGS-ALMA galaxies. Radii are slightly larger in NGC 3256 and free-fall times slightly shorter. However, the distribution of cloud eccentricities measured in NGC 3256 is often indistinguishable from those from the PHANGS-ALMA sample. Explanations for the similarities and differences across these properties are discussed in Section 5.

Despite differences in how the data were prepared, the mass function of clouds in NGC 3256 measured here appears roughly consistent in power-law slope with the independent analysis of these observations by Mok et al. (2020). Compared to the mass function shapes derived from the PHANGS-ALMA galaxies by Rosolowsky et al. (2021), the high-mass portion from NGC 3256 appears near the middle of their distribution of slopes.

Comparison of this analysis with a pixel-based approach used by Brunetti et al. (2021) shows general agreement between the measured

molecular-gas properties. Cloud and pixel-based analyses appear to be complementary in this case as the pixel analysis naturally does not require choosing what defines the edge of a “cloud”, while the cloud analysis can include more observed regions because of its ability to decompose multiple spectral components along the line of sight. Given the median cloud radius found here is 100 pc and the pixel analysis was performed with resolutions of 55, 80, and 120 pc, the pixel analysis was potentially resolving the clouds more than initially expected. The largest differences between the two methods appear to be related to the limitations imposed by the pixel-based analysis assuming clouds of a fixed size or having to avoid spectrally complex lines of sight.

Future observations of CO at even higher-resolution could begin to probe the gas properties within individual clouds. We could first search for signatures of the ISM becoming clumpier at resolutions below 55 pc. Given the high SFR in NGC 3256 there must eventually be a scale where the molecular gas decouples from its surroundings and would be observed to be collapsing. Observing gas within individual clouds would also likely reveal the small-scale properties that set the self-gravitating threshold density of the gas as well as the fraction of self-gravitating gas.

ACKNOWLEDGEMENTS

We are grateful to Dr. E. Rosolowsky for many helpful discussions about the details of how PYCPROPS works and on ways to match our analysis to that of PHANGS-ALMA. We are also grateful to Dr. G. Eadie for helpful discussion about logistic regression. We thank the anonymous referee for detailed comments that improved the content of this paper.

The research of NB is partially supported by the New Technologies for Canadian Observatories, an NSERC CREATE program. The research of CDW is supported by grants from the Natural Sciences and Engineering Research Council of Canada and the Canada Research Chairs program.

We acknowledge the use of the ARCADE (ALMA Reduction in the CANFAR Data Environment) science platform. ARCADE is a ALMA Cycle 7 development study with support from the National Radio Astronomy Observatory, the North American ALMA Science Centre, and the National Research Centre of Canada.

This research made use of ASTROPY, a community-developed core PYTHON package for Astronomy (<http://www.astropy.org>, Astropy Collaboration et al. 2013, 2018). This research also made use of the SCI-PY (Virtanen et al. 2020), MATPLOTLIB (Hunter 2007), NUMPY (van der Walt et al. 2011), PANDAS (McKinney 2010), SCIKIT-LEARN (Pedregosa et al. 2011), JUPYTER NOTEBOOK (Kluyver et al. 2016), and STATS MODELS (Seabold & Perktold 2010) PYTHON packages. This research has made use of the Cube Analysis and Rendering Tool for Astronomy (CARTA) (Comrie et al. 2021). This research has made use of NASA’s Astrophysics Data System. This research has made use of the Vizier catalogue access tool (Ochsenbein et al. 2000). This research has made use of the NASA/IPAC Extragalactic Database (NED), which is funded by the National Aeronautics and Space Administration and operated by the California Institute of Technology. This research has made use of the SIMBAD database, operated at CDS, Strasbourg, France (Wenger et al. 2000).

DATA AVAILABILITY

This paper makes use of the following ALMA data: ADS/JAO.ALMA#2015.1.00714.S (accessed from the ALMA Science portal at almascience.org). ALMA is a partnership of ESO (representing its member states), NSF (USA) and NINS (Japan), together with NRC (Canada), MOST and ASIAA (Taiwan), and KASI (Republic of Korea), in cooperation with the Republic of Chile. The Joint ALMA Observatory is operated by ESO, AUI/NRAO and NAOJ. The National Radio Astronomy Observatory is a facility of the National Science Foundation operated under cooperative agreement by Associated Universities, Inc.

The derived data generated in this research will be shared on reasonable request to the corresponding author.

REFERENCES

- Adamo A., et al., 2020, *MNRAS*, **499**, 3267
- Astropy Collaboration et al., 2013, *A&A*, **558**, A33
- Astropy Collaboration et al., 2018, *AJ*, **156**, 123
- Benincasa S. M., Wadsley J., Couchman H. M. P., Keller B. W., 2016, *MNRAS*, **462**, 3053
- Bolato A. D., Wolfire M., Leroy A. K., 2013, *ARA&A*, **51**, 207
- Braun R., Walterbos R. A. M., Kennicutt Robert C. J., Tacconi L. J., 1994, *ApJ*, **420**, 558
- Brunetti N., Wilson C. D., Sliwa K., Schinnerer E., Aalto S., Peck A. B., 2021, *MNRAS*, **500**, 4730
- Comrie A., et al., 2021, CARTA: The Cube Analysis and Rendering Tool for Astronomy, [doi:10.5281/zenodo.4905459](https://doi.org/10.5281/zenodo.4905459)
- Daddi E., et al., 2010, *ApJ*, **714**, L118
- Dobbs C. L., Burkert A., Pringle J. E., 2011, *MNRAS*, **413**, 2935
- Ellison S. L., Patton D. R., Simard L., McConnachie A. W., 2008, *AJ*, **135**, 1877
- Ellison S. L., Mendel J. T., Patton D. R., Scudder J. M., 2013, *MNRAS*, **435**, 3627
- Elmegreen B. G., 2011, *ApJ*, **737**, 10
- Elmegreen D. M., Elmegreen B. G., Marcus M. T., Shahinyan K., Yau A., Petersen M., 2009, *ApJ*, **701**, 306
- Elmegreen D. M., et al., 2021, *ApJ*, **908**, 121
- Field G. B., Blackman E. G., Keto E. R., 2011, *MNRAS*, **416**, 710
- Hani M. H., Gosain H., Ellison S. L., Patton D. R., Torrey P., 2020, *MNRAS*, **493**, 3716
- Harada N., Sakamoto K., Martín S., Aalto S., Aladro R., Sliwa K., 2018, *ApJ*, **855**, 49
- Herrero-Illana R., et al., 2019, *A&A*, **628**, A71
- Hollenbach D. J., Tielens A. G. G. M., 1999, *Reviews of Modern Physics*, **71**, 173
- Hopkins P. F., Quataert E., Murray N., 2012, *MNRAS*, **421**, 3488
- Howard C. S., Pudritz R. E., Harris W. E., 2017, *MNRAS*, **470**, 3346
- Hughes A., et al., 2013, *ApJ*, **779**, 44
- Hunter J. D., 2007, *Computing in Science & Engineering*, **9**, 90
- Iono D., Ho P. T. P., Yun M. S., Matsushita S., Peck A. B., Sakamoto K., 2004, *ApJ*, **616**, L63
- Kennicutt R. C., de los Reyes M. A. C., 2021, *ApJ*, **908**, 61
- Kluyver T., et al., 2016, in Loizides F., Schmidt B., eds, 20th International Conference on Electronic Publishing. Positioning and Power in Academic Publishing: Players, Agents and Agendas. IOS Press, Netherlands, p. 87
- Koda J., Sawada T., Hasegawa T., Scoville N. Z., 2006, *ApJ*, **638**, 191
- Kruijssen J. M. D., 2012, *MNRAS*, **426**, 3008
- Krumholz M. R., Matzner C. D., McKee C. F., 2006, *ApJ*, **653**, 361
- Krumholz M. R., Burkhardt B., Forbes J. C., Crocker R. M., 2018, *MNRAS*, **477**, 2716
- Larson R. B., Tinsley B. M., 1978, *ApJ*, **219**, 46
- Larson K. L., et al., 2020, *ApJ*, **888**, 92
- Leroy A. K., et al., 2016, *ApJ*, **831**, 16
- Louvet F., Hennebelle P., Men'shchikov A., Didelon P., Ntormousi E., Motte F., 2021, *A&A*, **653**, A157
- Madau P., Dickinson M., 2014, *ARA&A*, **52**, 415
- McKee C. F., 1989, *ApJ*, **345**, 782
- McKee C. F., Ostriker J. P., 1977, *ApJ*, **218**, 148
- McKinney W., 2010, in Stéfan van der Walt Jarrod Millman eds, Python in Science Conf. Ser.. Available at: <http://conference.scipy.org/proceedings/scipy2010/>, p. 56
- Mihos J. C., Hernquist L., 1996, *ApJ*, **464**, 641
- Mok A., Chandar R., Fall S. M., 2020, *ApJ*, **893**, 135
- Narayan C. A., Jog C. J., 2002, *A&A*, **394**, 89
- Noguchi M., 1988, *A&A*, **203**, 259
- Ochsenein F., Bauer P., Marcout J., 2000, *A&AS*, **143**, 23
- Ohya Y., Terashima Y., Sakamoto K., 2015, *ApJ*, **805**, 162
- Ostriker E. C., Shetty R., 2011, *ApJ*, **731**, 41
- Pedregosa F., et al., 2011, *Journal of Machine Learning Research*, **12**, 2825
- Pineda J. E., Rosolowsky E. W., Goodman A. A., 2009, *ApJ*, **699**, L134
- Reid M. A., Wilson C. D., 2006a, *ApJ*, **644**, 990
- Reid M. A., Wilson C. D., 2006b, *ApJ*, **650**, 970
- Reid M. A., Wadsley J., Petitclerc N., Sills A., 2010, *ApJ*, **719**, 561
- Romano M., et al., 2021, *A&A*, **653**, A111
- Rosolowsky E., Leroy A., 2006, *PASP*, **118**, 590
- Rosolowsky E., et al., 2021, *MNRAS*, **502**, 1218
- Rots A. H., 1978, *AJ*, **83**, 219
- Sakamoto K., Aalto S., Combes F., Evans A., Peck A., 2014, *ApJ*, **797**, 90
- Sánchez S. F., et al., 2014, *A&A*, **563**, A49
- Sánchez S. F., et al., 2019, *MNRAS*, **484**, 3042
- Scholz F. W., Stephens M. A., 1987, *Journal of the American Statistical Association*, **82**, 918
- Scott D. W., 1992, *Multivariate Density Estimation: Theory, Practice, and Visualization*. Wiley Series in Probability and Statistics, John Wiley & Sons, New York
- Seabold S., Perktold J., 2010, in van der Walt S., Millman J., eds, Python in Science Conf. Ser.. Available at: <http://conference.scipy.org/proceedings/scipy2010/>
- Shetty R., Ostriker E. C., 2012, *ApJ*, **754**, 2
- Soida M., Urbanik M., Beck R., Wielebinski R., Balkowski C., 2001, *A&A*, **378**, 40
- Solomon P. M., Rivolo A. R., Barrett J., Yahil A., 1987, *ApJ*, **319**, 730
- Stierwalt S., et al., 2013, *ApJS*, **206**, 1
- Sun J., et al., 2018, *ApJ*, **860**, 172
- Sun J., et al., 2020a, *ApJ*, **892**, 148
- Sun J., et al., 2020b, *ApJ*, **901**, L8
- Tacconi L. J., Genzel R., Sternberg A., 2020, *ARA&A*, **58**, 157
- Tielens A. G. G. M., Hollenbach D., 1985, *ApJ*, **291**, 722
- Virtanen P., et al., 2020, *Nature Methods*, **17**, 261
- van der Walt S., Colbert S. C., Varoquaux G., 2011, *Comput. Sci. Eng.*, **13**, 22
- Wenger M., et al., 2000, *A&AS*, **143**, 9
- Wilson C. D., Elmegreen B. G., Bemis A., Brunetti N., 2019, *ApJ*, **882**, 5
- Yamashita T., et al., 2017, *ApJ*, **844**, 96
- Zaragoza-Cardiel J., Smith B. J., Rosado M., Beckman J. E., Bitsakis T., Camps-Fariña A., Font J., Cox I. S., 2018, *ApJS*, **234**, 35

APPENDIX A: EFFECT OF PIXEL SIZE ON VELOCITY-DISPERSION DISTRIBUTIONS

Since the spatial pixel size of interferometric cubes is a free parameter during imaging and cleaning, we originally chose to have about five pixels across the native beam FWHM of ≈ 47 pc to safely oversample each resolution element. Cubes were then convolved to have a range of larger beam sizes, and before the pixel-based analysis by Brunetti et al. (2021) the cubes were regridded to have two pixels across each beam FWHM to roughly Nyquist sample each resolution element. When trying to decide what pixel size to use for this cloud-finding analysis, we compared results with a range of pixel sizes from 2 to

almost 14 pixels across the beam FWHM at different spatial resolutions. We initially intended to use the cube with two pixels across the beam to make comparisons with our previous pixel analysis more direct, but we found the distribution of velocity dispersions changed with the choice of pixel size, regardless of spatial resolution.

Figure A1 shows how the cloud velocity-dispersion distributions, medians, and inner 68th percentile ranges change with pixel size at a range of spatial resolutions. Two and five pixels across each beam FWHM were tested, along with eight if possible, and finally the smallest pixels came from not regridding the cubes after imaging with the native 47 pc beam. Across all resolutions, the medians are lower for larger pixels (e.g. fewer pixels across the beam FWHM) and potentially show signs of convergence towards the smallest pixels. These cloud-finding tests were carried out on cubes that did not have homogenized noise so it is best to compare the distributions at a single spatial resolution to avoid lower noise levels at poorer resolution influencing the cloud properties. Between pixel sizes, the standard error on the mean noise RMS was at most half a per cent of the median RMS, so the changes in the distributions are not likely driven by the changing noise level.

Visual inspection of the cloud boundaries suggests that the change in velocity-dispersion distributions was because the boundaries between clouds changed with changing pixel size. Figure A2 shows a small grouping of clouds to the north of the nuclei along a spiral-arm feature, where the emission was relatively isolated so the cloud boundaries should be easiest to follow through the cube. The smallest pixels result in some clouds remaining spatially distinct over more velocity channels. In contrast, larger pixels sometimes resulted in the boundary between two clouds shifting in the spatial dimensions while moving along the spectral dimension. These shifting boundaries resulted in the emission at one spatial location being split between two clouds along the velocity dimension, so that one cloud “wrapped around” a spatially adjacent one in velocity. This wrapping scenario is visible for the cloud marked with an arrow in Figure A2, where the arrow is drawn at the same location at each velocity slice and at both pixel sizes.

Also visible in Figure A2 is how the cloud to the left of the arrow splits into two clouds by the 2842 km s⁻¹ panel with large pixels but remains a single cloud at all velocities with smaller pixels. A noise peak/trough combined with large pixels could result in a larger gradient, causing the emission to be split into more than one cloud. However, smaller pixels may better resolve the same feature as a smooth gradient along the cloud so it does not split. Both the wrapping and splitting along the velocity axis in the 2 pixel version will result in lower velocity dispersions since the clouds span fewer channels.

Given the main point of comparison in this work is to the PHANGS-ALMA cloud-finding results from [Rosolowsky et al. \(2021\)](#), we chose to match spatial resolution by carrying out the remainder of our analysis on the 90 pc resolution cube. As for pixel size, we chose to use the smallest pixels we could with a cube that was derived from the same imaging by [Brunetti et al. \(2021\)](#). Changes in the velocity-dispersion distributions, medians, and inner 68th percentile ranges decrease as the number of pixels across the beams increase, possibly indicating the measurements with small pixels are closer to converged/“true” values. Smaller pixels also have the benefit of reducing the amount of velocity wrapping and splitting of the found clouds.

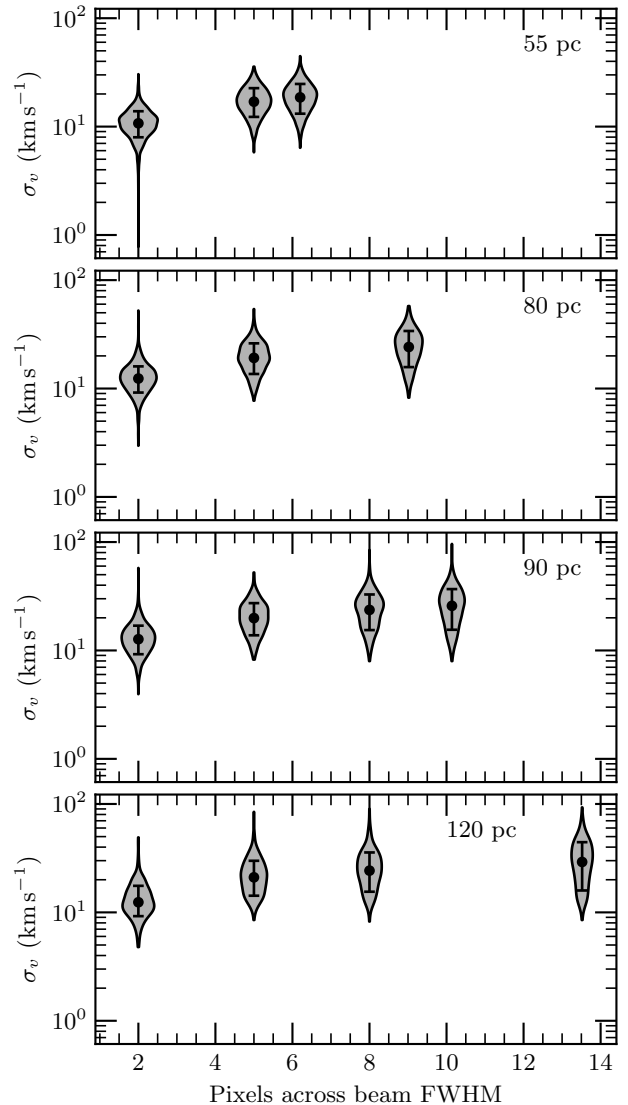


Figure A1. Distributions of cloud velocity dispersions vs. pixel size (measured in the number of pixels across the beam FWHM) with results at different spatial resolutions shown in each row. Circles show medians and errorbars show 16th to 84th percentile ranges. Curves and shaded regions show Gaussian KDEs, with uniform weights for all clouds and widths normalized across all distributions to show relative cloud fractions per dex.

APPENDIX B: ADDITIONAL SCALING-RELATION VIEWS

Presented here are the same scaling relations shown in Figures 9 through 12 but highlighting some additional features. In Figure B1, the colour of the points from NGC 3256 now indicates the distance from the cloud centre to one of the progenitor nuclei. The distance to both nuclei was calculated for each cloud and the smaller distance is used to colour the points. Positions of the nuclei are the same as used by [\(Brunetti et al. 2021\)](#) and are R.A. 10^h27^m51^s.226 Dec. -43°54′13″.942 for the northern nucleus and R.A. 10^h27^m51^s.221 Dec. -43°54′19″.168 for the southern nucleus. Generally, clouds with the highest values for any of the properties shown are found closer to the nuclei while most of the rest of the distributions are at a mix of distances.

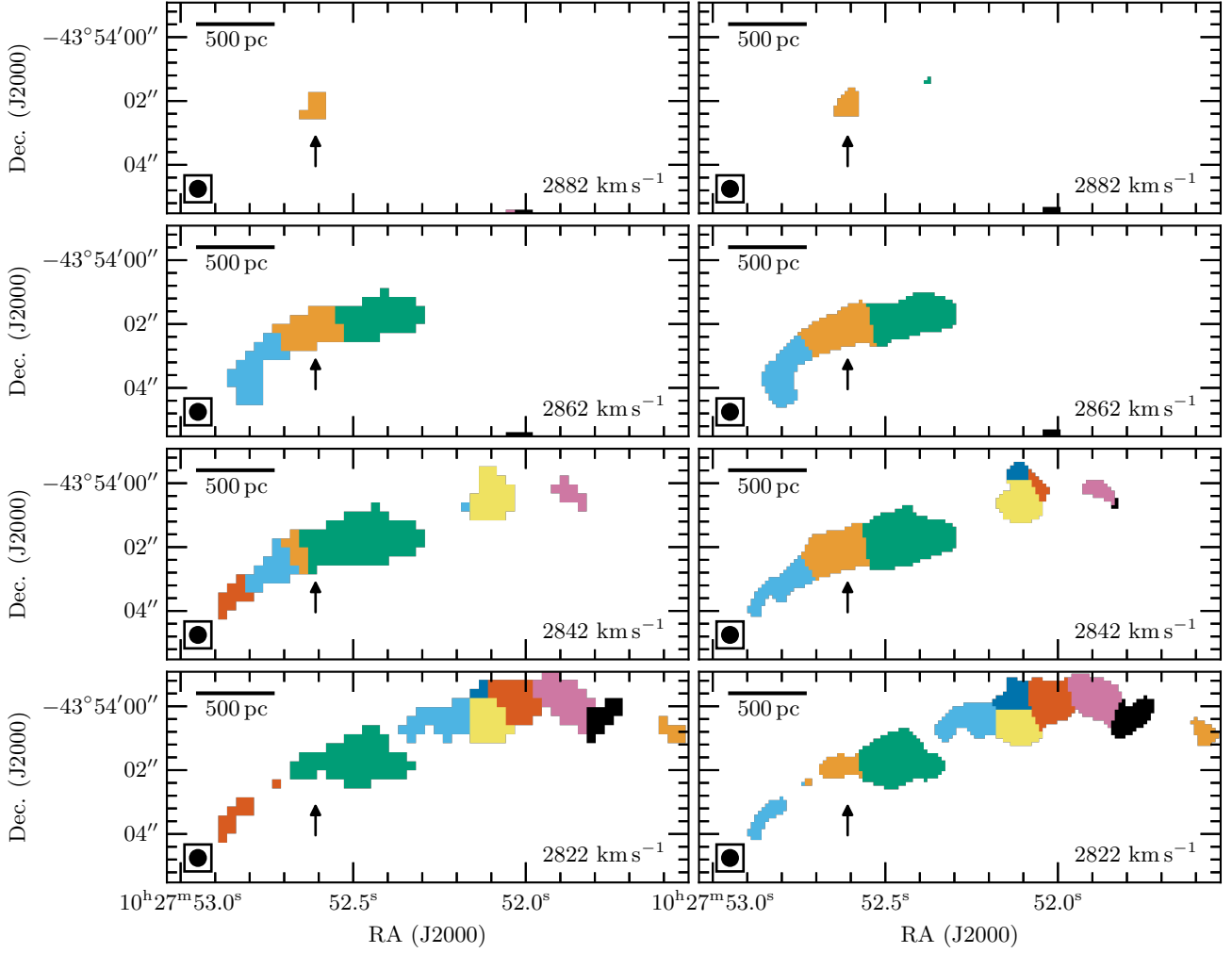


Figure A2. Spatial maps at 120 pc resolution showing identified clouds labelled by colour and at different velocity slices (rows) when the emission cube was regridded to have two (left) and five (right) pixels across the beam FWHM. Velocities of the slices are shown in the bottom-right of each panel, the beam size is shown as the black circles in the bottom-left, and a scale bar in the top-left indicates 500 pc at the distance of NGC 3256. Arrows in each panel highlight a cloud that with large pixels has the adjacent cloud to the right “wrap around” it along the velocity axis so its velocity range is reduced, but with small pixels both clouds persist along the same range in velocity. Also note how the cloud to the left of the arrow splits into two clouds across this velocity range with large pixels but is identified as a single cloud throughout with small pixels.

To explore if it is always the same clouds in NGC 3256 that are most consistent with PHANGS-ALMA throughout Figures 9 through 12, we have highlighted clouds either with the smallest values of velocity dispersion or two-dimensional radius in Figure B2. The criteria are easiest to see in the top-left panel as clouds that had $\sigma_v < 17 \text{ km s}^{-1}$ are in green and $R < 60 \text{ pc}$ are in red. The colour for clouds that met both of the criteria was chosen by the quantity with the larger per cent difference from the corresponding threshold. For example, a cloud with a velocity dispersion of 2 km s^{-1} and two-dimensional radius of 40 pc would be shown in green. Broadly, those two groups are typically the clouds that are most similar to PHANGS-ALMA or their trends. This is not true, however, for small-radius clouds in the velocity dispersion vs. radius and size-linewidth coefficient vs. mass surface density plots, where clouds from NGC 3256 appear where there are no clouds from PHANGS-ALMA.

This paper has been typeset from a \LaTeX file prepared by the author.

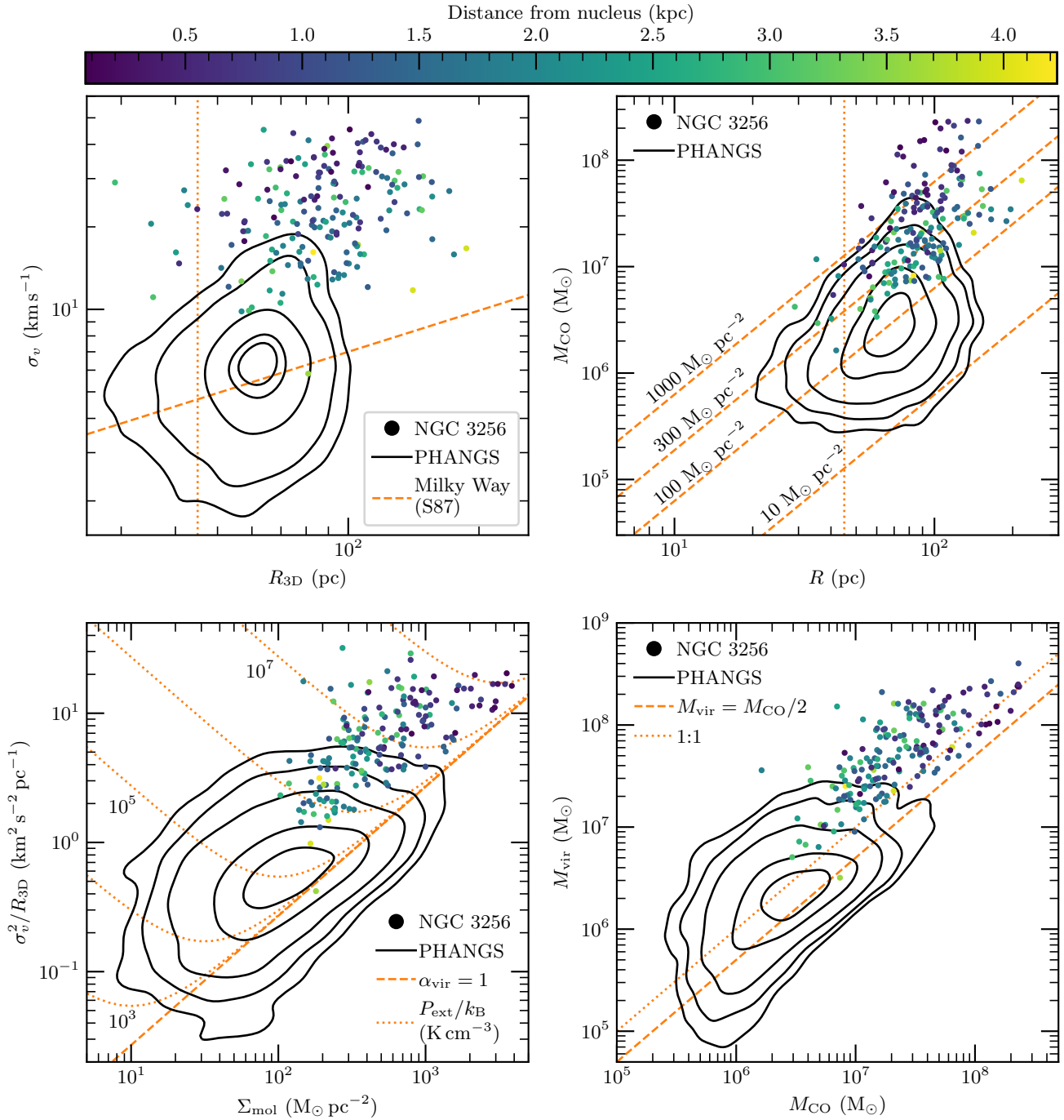


Figure B1. Same as Figures 9 through 12 but now the points from the NGC 3256 clouds are coloured by their distance from one of the progenitor nuclei. The smaller of the two distances from the northern or southern nucleus is shown. Positions of the nuclei are R.A. $10^{\text{h}}27^{\text{m}}51^{\text{s}}.226$ Dec. $-43^{\circ}54'13''.942$ for the northern nucleus and R.A. $10^{\text{h}}27^{\text{m}}51^{\text{s}}.221$ Dec. $-43^{\circ}54'19''.168$ for the southern nucleus.

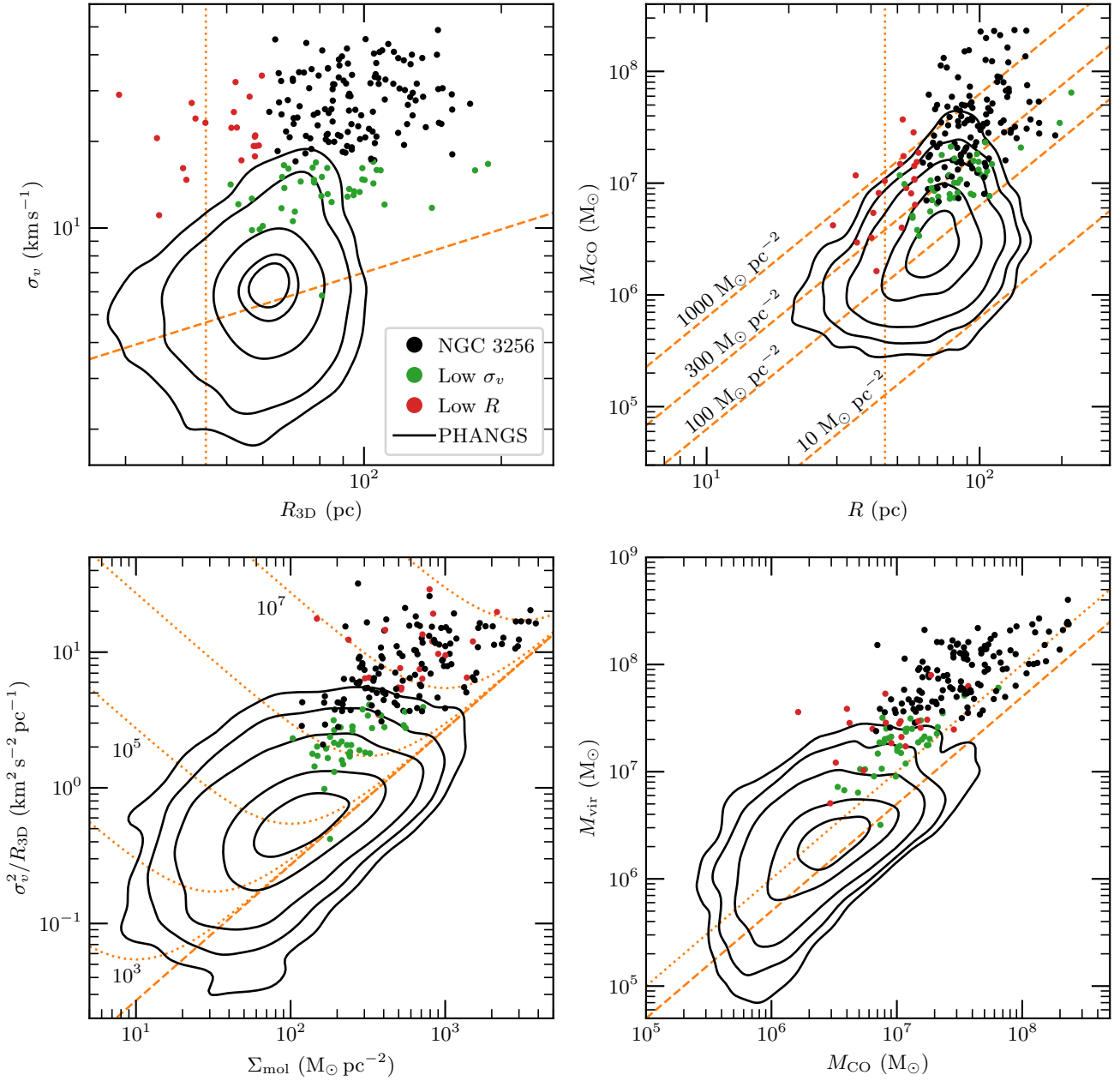


Figure B2. Same as Figures 9 through 12 but clouds with small velocity dispersions or radii marked with colour in each panel. Green points show clouds with $\sigma_v < 17$ km s⁻¹ and red points show clouds with $R < 60$ pc. If a cloud met both of the criteria then the colour was chosen based on which property has the largest per cent difference from the threshold.